Comparison of the Analyses and Forecasts of a Tornadic Supercell Storm from Assimilating Phased-Array Radar and WSR-88D Observations

TIMOTHY A. SUPINIE

Center for Analysis and Prediction of Storms, University of Oklahoma, Norman, Oklahoma

NUSRAT YUSSOUF

Cooperative Institute for Mesoscale Meteorological Studies, University of Oklahoma, and NOAA/OAR/National Severe Storms Laboratory, Norman, Oklahoma

YOUNGSUN JUNG AND MING XUE

Center for Analysis and Prediction of Storms, University of Oklahoma, Norman, Oklahoma

JING CHENG

Cooperative Institute for Mesoscale Meteorological Studies, University of Oklahoma, and NOAA/OAR/National Severe Storms Laboratory, Norman, Oklahoma

SHIZHANG WANG

Nanjing University, Nanjing, China

ABSTRACT

NOAA's National Severe Storms Laboratory is actively developing phased-array radar (PAR) technology, a potential next-generation weather radar, to replace the current operational WSR-88D radars. One unique feature of PAR is its rapid scanning capability, which is at least 4–5 times faster than the scanning rate of WSR-88D. To explore the impact of such high-frequency PAR observations compared with traditional WSR-88D on severe weather forecasting, several storm-scale data assimilation and forecast experiments are conducted. Reflectivity and radial velocity observations from the 22 May 2011 Ada, Oklahoma, tornadic supercell storm are assimilated over a 45-min period using observations from the experimental PAR located in Norman, Oklahoma, and the operational WSR-88D radar at Oklahoma City, Oklahoma. The radar observations are assimilated into the ARPS model within a heterogeneous mesoscale environment and 1-h ensemble forecasts are generated from analyses every 15 min. With a 30-min assimilation period, the PAR experiment is able to analyze more realistic storm structures, resulting in higher skill scores and higher probabilities of low-level vorticity that align better with the locations of radar-derived rotation compared with the WSR-88D experiment. Assimilation of PAR observations for a longer 45-min time period generates similar forecasts compared to assimilating WSR-88D observations, indicating that the advantage of rapid-scan PAR is more noticeable over a shorter 30-min assimilation period. An additional experiment reveals that the improved accuracy from the PAR experiment over a shorter assimilation period is mainly due to its high-temporal-frequency sampling capability. These results highlight the benefit of PAR's rapid-scan capability in storm-scale modeling that can potentially extend severe weather warning lead times.

1. Introduction

Since 2003, engineers and scientists at the National Oceanic and Atmospheric Administration's (NOAA) National Severe Storms Laboratory (NSSL) have been actively working on the applications for phased-array radar (PAR) technology, a potential replacement candidate for the current operational Weather Surveillance Radar-1988 Doppler (WSR-88D) network across the United States (Weber et al. 2007; Zrnić et al. 2007;

Corresponding author: Timothy A. Supinie, tsupinie@ou.edu

Heinselman and Torres 2011; Curtis and Torres 2011). An experimental S-band PAR research radar is located at the National Weather Radar Testbed (NWRT) in Norman, Oklahoma (Forsyth et al. 2005), and has been used to explore the feasibility of this technology for severe weather applications. There are several significant differences between the NWRT PAR and WSR-88D technology. While the WSR-88D collects data over a 360° azimuthal sector with a fixed 0.95° beamwidth, the NWRT PAR, containing only a single panel at this time, scans only up to a 90°-wide sector and the beamwidth varies with azimuth (from 1.6° at boresight to 2.3° at ±45° off boresight). Thus, the WSR-88D observations have a larger spatial coverage area and higher spatial resolution compared with the PAR observations. However, one unique feature of PAR technology that makes it very attractive to the field of meteorology is its electronic steering ability, which enables it to scan one complete volume of observations in less than a minute (Heinselman and Torres 2011). In contrast, the WSR-88D takes about 4.5 min to scan one complete volume of observations because of its mechanically steered beam.

Several studies during the past decade have demonstrated the advantages of high-temporal-resolution NWRT PAR observations in better understanding rapidly evolving complex features of a variety of severe convective systems ranging from microbursts, hailstorms with associated lightning activity (Heinselman et al. 2008; Emersic et al. 2011), quasi-linear convective systems (Newman and Heinselman 2012), and tornadic supercell storms (Tanamachi et al. 2015). In addition, the Phased Array Radar Innovative Sensing Experiments (PARISE) conducted at NSSL over the past several years show that the rapid volumetric PAR observations of ongoing convection more closely match the NWS forecasters' conceptual models of storm evolution compared with 4–5-min volumetric updates provided by the operational WSR-88Ds (Heinselman et al. 2012, 2015; Bowden et al. 2015). The rapid-scan PAR observations also increase the forecasters' situational awareness, resulting in longer tornado warning lead times compared with the traditional WSR-88D radar updates (Heinselman et al. 2012, 2015; Kuster et al. 2015). While the rapid-scan PAR observations have already shown promise toward improved understanding of convective weather and longer severe weather warning lead times, there is also considerable interest in evaluating the impact of the rapid-scan capability of PAR in storm-scale numerical weather prediction (NWP) as compared with the WSR-88Ds. This evaluation is particularly important within the context of NOAA's Warn-on-Forecast (WoF; Stensrud et al. 2009, 2013) program, which envisions incorporating storm-scale NWP models into the severe weather warning-decision process of NWS operational forecasting.

One advanced data assimilation (DA) approach for storm-scale NWP is the ensemble Kalman filter (EnKF; Evensen 1994), with the ensemble square root filter (EnSRF; Whitaker and Hamill 2002) being one of the most popular variants. Results from studies during the past decade show that assimilating WSR-88D observations using EnSRF in both homogeneous, single-sounding idealized frameworks (e.g., Snyder and Zhang 2003; Dowell et al. 2004; Tong and Xue 2005; Xue et al. 2006; Aksoy et al. 2009, 2010; Yussouf and Stensrud 2010, 2012; Dowell et al. 2011; Dawson et al. 2012) and heterogeneous mesoscale environments (e.g., Lei et al. 2009; Dowell et al. 2010; Snook et al. 2011, 2012; Jung et al. 2012; Yussouf et al. 2013; Putnam et al. 2014; Wheatley et al. 2014; Snook et al. 2015; Yussouf et al. 2015) creates a good representation of convection in both analyses and forecasts. However, the impact of assimilating high-temporal-resolution PAR observations in NWP models for severe weather forecasting is not clear. Yussouf and Stensrud (2010) conducted several observing system simulation experiments (OSSEs) using an EnSRF data assimilation technique and demonstrated that, with only a short 15-min data assimilation period, assimilating high-temporal-frequency PAR observations yields significantly better analyses and ensemble forecasts than those produced using WSR-88D observations. The findings of Yussouf and Stensrud (2010) are consistent with the findings of Xue et al. (2006), who also found that simulated radar scan volumes at 1-min intervals significantly shorten the time needed to obtain good analyses of a convective storm.

However, the OSSEs conducted in both of the above studies are based on a perfect model assumption in which model error does not play a role. Given the idealized nature of such OSSE studies, their results may be too optimistic, although they do provide an upper-limit estimate of the benefit of rapid-scan PAR in NWP. Demonstrating similar impacts using real PAR observations in a realistic atmospheric environment is more challenging, where model errors are inevitable and can arise from inaccuracies in model physics parameterizations, insufficient resolution, numerical approximations, errors in initial and boundary conditions, etc. (Aksoy et al. 2009, 2010; Potvin and Wicker 2013). Moreover, assimilating such high-temporal-frequency PAR observations using the three-dimensional (3D) EnSRF technique involves shorter assimilation cycles of 1 min or less, which are computationally very expensive. In addition, the frequent stopping and restarting of the model

with a very short assimilation frequency can potentially introduce imbalances and can generate noise in the prediction system every time a new analysis is performed (S. Wang et al. 2013; Lange and Craig 2014). On the other hand, using longer assimilation cycles (10 min or more) can save computational cost and avoid imbalances due to frequent model updates. But using longer assimilation cycles with a 3D EnKF algorithm can introduce data timing errors when the observations taken at different times within the assimilation windows are assumed to be valid at the analysis time. If observations away from the analysis time are discarded, important features associated with the evolving storms may be missed, leading to poorer analyses and forecasts.

To counteract these problems with 3D EnKF, Sakov et al. (2010) proposed a generic asynchronous or four-dimensional (4D) EnKF called AEnKF that allows for the assimilation of observations distributed over time. The algorithm involves calculating updates using observations from the time of actual observation rather than from the time of analysis, as in the traditional 3D EnKF. Therefore, the AEnKF technique is able to utilize more observations collected over time with fewer analysis cycles, reducing the frequent model stopping and restarting.

Recently, S. Wang et al. (2013) developed a 4D asynchronous implementation of the EnSRF (which they called 4DEnSRF) that is most commonly used for storm-scale radar DA. They tested the 4DEnSRF technique for radar DA using OSSEs with assimilation cycle lengths ranging from 1 to 20 min. The results indicate that 4DEnSRF outperforms the traditional 3D EnSRF when the assimilation cycle frequency is longer than 1 min (S. Wang et al. 2013). The 4DEnSRF technique assimilates high-frequency observations distributed over a specified time interval using a single update, thereby reducing the number of analysis cycles, which is desirable for reducing the computational cost and potential noise generation. This advantage of the 4DEnSRF technique in handling high-temporal-frequency observations is attractive for PAR DA.

To evaluate and compare the impact of assimilating rapid-scan PAR and the traditional WSR-88D observations in storm-scale severe weather forecasting, several 4DEnSRF DA and forecast experiments are conducted using WSR-88D, rapid-scan PAR, and PAR observations subsampled at a WSR-88D-like temporal resolution. The study is conducted within a heterogeneous mesoscale environment using the 22 May 2011 Ada, Oklahoma, tornadic supercell event. The radar observations are assimilated every 5 min for a 45-min-long assimilation period prior to tornadogenesis, and 1-h

TABLE 1. Tornado reports associated with storm B on 22 May 2011 obtained from the Storm Prediction Center (http://www.spc.noaa.gov/climo/reports/110521_rpts.html).

Time (UTC)	Location	County in OK	Lat (°)	Lon (°)
0119	3.22 km NW Vanoss	Pontotoc	34.79	−96.89
0130	12.88 km W Ada	Pontotoc	34.78	−96.80
0134	8.05 km W Ada	Pontotoc	34.78	−96.75
0141	6.44 km WNW Ada	Pontotoc	34.80	−96.73

ensemble forecasts are launched after 15, 30, and 45 min of radar DA. The goal is to see if the findings from the OSSE study of Yussouf and Stensrud (2010) hold true in a realistic mesoscale environment using real radar observations.

The rest of this paper is organized as follows. A brief description of the supercell event is documented in section 2. Section 3 describes the experiment design and the radar observations used in the DA and forecast experiments. Section 4 presents the results and discussions, followed by a summary in section 5.

2. Overview of the 22 May 2011 Ada, Oklahoma, tornadic supercell event

The 22 May 2011 Ada, Oklahoma, tornadic supercell was a weakly tornadic event with a tornado rating of EF0 on the enhanced Fujita (EF) scale. The tornadoes started at ~0119 UTC and ended at ~0141 UTC (based on tornado reports; Table 1). Several operational WSR-88D radars and the NWRT PAR documented the life cycle of this supercell storm. During the late afternoon and evening of 21 May 2011, a dryline extended from the Big Bend area of Texas (southwest Texas) through central Oklahoma and into south-central Kansas where it intersected the Pacific front. A midlevel jet rotating through the base of an upper low increased the effective shear. The bulk wind difference through 0–6 km AGL in the 0000 UTC 22 May 2011 Norman, Oklahoma, sounding was 43 kt ($22.1 \, \mathrm{m \, s^{-1}}$); values greater than 40 kt ($20.6 \, \mathrm{m \, s^{-1}}$) favor supercell storms. Convection initiated along the dryline in south-central Oklahoma, and by 0000 UTC on 22 May, a storm (storm A) evolved into a supercell in south-central Oklahoma (Fig. 1a). Several smaller cells developed north of storm A (Figs. 1a–c), and the one (storm B) closest to storm A matured into a supercell with a hook echo feature by 0045 UTC (Fig. 1d). There was one tornado report associated with storm A at 0040 UTC in Murray County, Oklahoma (SPC storm report database). During the next 30 min, storm B grew stronger, and storm A quickly dissipated when it encountered storm B (Figs. 1e–h). There were
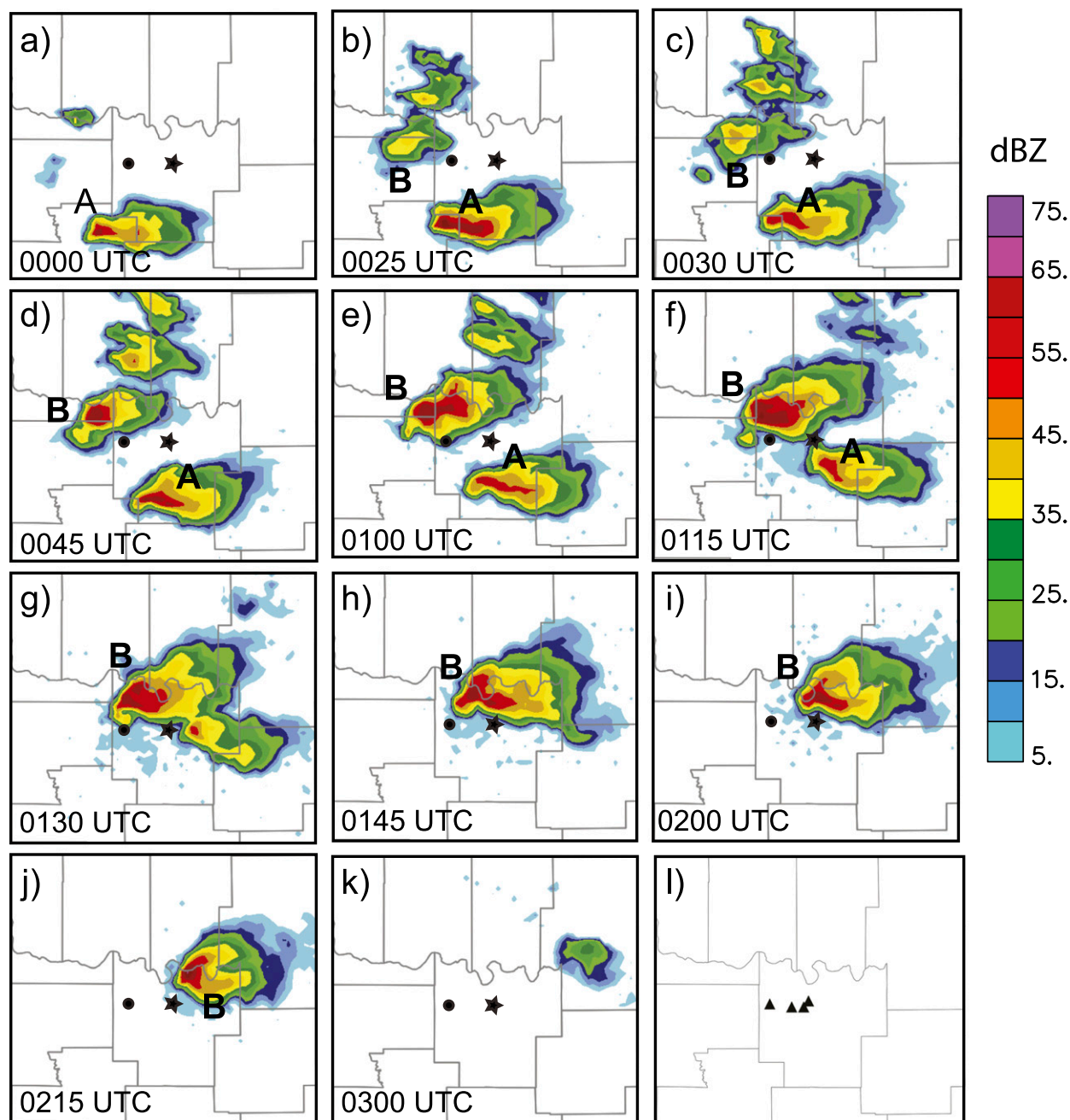
FIG. 1. Observed reflectivity (dB*Z*, from the NSSL NMQ system) at 2 km MSL at (a) 0000, (b) 0025, (c) 0030, (d) 0045, (e) 0100, (f) 0115, (g) 0130, (h) 0145, (i) 0200, (j) 0215, and (k) 0215 UTC 22 May 2011 over the area of interest. The black circle indicates the location of Vanoss and the black star indicates the location of Ada. (l) The black triangles are the four tornado reports from storm B (Table 1).

four tornado reports (Table 1) associated with storm B, all of which were rated as 0 on the EF scale. The first tornado report was at 0119 UTC and located 3.2 km northwest of Vanoss, Oklahoma. The supercell continued east toward Ada. The last tornado report from storm B was at 0141 UTC, located 6.44 km west-northwest of Ada. There is no damage track available for this event. The storm starts to dissipate after 0200 UTC (Figs. 1i–k). The storms were sampled by both WRD-88D radars and NWRT PAR. The observations from both radar platforms are assimilated separately into a storm-scale ensemble forecast system in order to compare the ability of the radars in forecasting the storm and its associated low-level mesocyclone.

3. Data, model, and experiment design

a. The WSR-88D (KTLX) observations

The storm associated with the Ada tornado was ~80 km away from the operational WSR-88D radar at Twin Lakes, Oklahoma (KTLX). The WSR-88D radar sampled the storm at ~4.2-min intervals with a volume coverage pattern that consisted of 14 tilts (elevation angles) ranging from 0.46° to 19.45° (Table 2). The level II reflectivity and radial velocity observations from the WSR-88D at KTLX are quality controlled using an automatic procedure within the Advanced Regional Prediction System (ARPS) package to eliminate noise and ground clutter from the reflectivity observations and to unfold the aliased radial velocity observations (Brewster et al. 2005). The quality controlled reflectivity and radial velocity observations from both radars are interpolated onto the model grid horizontally, but remain on the radar elevation levels vertically; this procedure is used in many real-data studies with the ARPS EnKF DA system (e.g., Jung et al. 2012; Snook et al. 2012).

b. The NWRT PAR observations

The NWRT PAR sampled the evolution of the Ada supercell with a 90° sector at a rapid ~50 s for volume updates. The volume coverage pattern spanned tilts from 0.5° to 60° with a higher number of tilts at lower levels of the atmosphere. In this study, the lowest 14 elevation angles from 0.5° to 19.5° are assimilated (Table 3) into the model during the 45-min DA period. However, because of mechanical failures, several volume scans of NWRT PAR observations are missing between 0045 and 0108 UTC (listed in Table 3) and therefore are not assimilated in the experiments. The NWRT PAR observations are quality controlled using the same ARPS quality control package and interpolated in the same manner as the WSR-88D observations.

There are a few caveats to using the PAR data. The first is that the scan sector is free to change between volume scans; this occurs twice for this case. The first and most substantial change occurs between the 0045 and 0050 UTC analyses, when the sector shifts approximately 21° counterclockwise. The second sector change is between the 0050 and 0055 UTC analyses; the scan sector shifts a further 2° counterclockwise. The effect of a sector change is that storms that were outside of the radar coverage area are now observed by the radar, which affects the observation space statistics. This will be discussed in more detail in later sections. In addition, because the PAR scans over a limited sector in azimuth, there is no way to suppress spurious convection outside the scan sector from the PAR. This can result in spurious convection interacting with the assimilated storms and degrading the quality of the forecast. To mitigate this, the zero-reflectivity observations from the most recent KTLX volume are used outside the PAR scan sector in the following manner. If the composite reflectivity from KTLX is less than or equal to 0 dBZ, the corresponding column of PAR observations is set to 0 dBZ. Otherwise, the entire column of PAR observations is set to "missing."

c. The mesoscale ensemble DA and forecast

The storm-scale radar DA experiments are performed on a grid with 2-km grid spacing, nested within a mesoscale grid of 18-km grid spacing that covers the continental United States (CONUS; Fig. 2a). ARPS (Xue et al. 2000, 2001, 2003) is used as the prediction model for the DA and forecast experiments while the EnSRF system developed for the ARPS system (Xue et al. 2006; Jung et al. 2012; Snook et al. 2012, 2015; Y. Wang et al. 2013; Putnam et al. 2014) and extended to the 4DEnSRF algorithm (S. Wang et al. 2013) is used for the ensemble DA.

The mesoscale domain contains $243 \times 163 \times 51$ grid points over the continental United States (Fig. 2a). The vertical grids are stretched with a vertical spacing of 50 m near the surface and 900 m at the model top. The model top is at 25 km with a Rayleigh damping layer above 12 km. A 40-member mesoscale ensemble is initialized from the 20-member National Centers for Environmental Prediction (NCEP) Short-Range Ensemble Forecasting (SREF; Du et al. 2006) analyses (at 40-km horizontal grid spacing) at 2100 UTC 21 May 2011, but using two sets of physics parameterizations (Table 2). The schemes used in the first set of 20 ensemble members are the Betts—Miller–Janjić cumulus parameterization scheme (Betts 1973) and the Sun and Chang TKE-based planetary boundary layer (PBL; Sun and Chang 1986; Xue et al. 1996) scheme. The remaining 20 ensemble members use the Kain–Fritsch cumulus parameterization scheme (Kain and Fritsch 1990, 1993) and the Yonsei University (YSU) PBL scheme (Hong and Pan 1996). In addition, the single-moment Lin (Lin et al. 1983) microphysics scheme, stability-dependent surface-layer physics, a two-layer soil model initialized from NCEP's Eta Model analysis, and the National Aeronautics and Space Administration (NASA) Goddard Space Flight Center (GSFC) (Chou 1990, 1992; Chou and Suarez 1994) long- and shortwave radiation schemes are used in all 40 ensemble members except for differences in the transmission functions used. The transmission function in the radiation scheme is computed using the k-distribution method for the first 20 members and using a lookup table for the remaining 20 ensemble members. The physics diversity in the mesoscale

TABLE 2. Physics options for the 40-member ARPS mesoscale and storm-scale ensemble system.

Parameterization scheme	Mesoscale ensemble members 1–20	Mesoscale ensemble members 21–40	Storm-scale ensemble members 1–40
Cumulus	Betts–Miller–Janjić	Kain–Fritsch	—
PBL	Sun and Chang	YSU	YSU
Long- and shortwave radiation	NASA GSFC; transmission functions are computed using the k-distribution method	NASA GSFC; transmission functions are computed using lookup table	NASA GSFC; transmission functions are computed using the k-distribution method
Cloud microphysical scheme	Lin scheme	Lin scheme	MY two-moment scheme

ensemble is used to represent model error in the ensemble system and to help account for ensemble underdispersion in the assimilation system (Yussouf and Stensrud 2012; Snook et al. 2012). This mesoscale ensemble is used to provide initial and boundary conditions for the one-way nested storm-scale ensemble system.

Routinely available surface (i.e., horizontal u and v wind components, temperature T, and dewpoint T_d), wind profiler (u and v), and radiosondes (u, v, potential temperature θ and T_d; only available at 0000 UTC 22 May 2011) observations are assimilated into the mesoscale domain every 1 h starting from 2200 UTC 21 May 2011 out to 0000 UTC 22 May 2011 (Fig. 2b) using the ARPS EnSRF (Xue et al. 2006; Y. Wang et al. 2013) system. Radar data are not assimilated onto the mesoscale grid. The covariance localization function is based on the fifth-order correlation function from Gaspari and Cohn (1999) with a horizontal cutoff radius of 300 km and 800 km used for the surface and upper-air (both wind profiler and radiosonde) observations, respectively. A 6-km cutoff radius in the vertical is used for all observations (Snook et al. 2015). To help maintain the ensemble spread, multiplicative inflation (Anderson 2001) with a factor of 5% is applied everywhere in the model domain to all model state variables. The mesoscale ensemble analyses at 0000

UTC are used to create the initial conditions for the storm-scale ensemble. Meanwhile, 2-h ensemble forecasts are generated from the mesoscale ensemble analyses at 0000 UTC 22 May 2011 out to 0200 UTC 22 May 2011 to provide ensemble boundary conditions for the storm-scale ensemble.

d. Storm-scale ensemble DA and forecast

The physics packages used by the ARPS on the 2-km nested grid are the same as the first 20 members of the mesoscale ensemble, except that the double-moment Milbrandt and Yau (2006a,b, hereafter MY) microphysics scheme and the YSU PBL scheme are used, while the cumulus parameterization scheme is turned off (Table 2).

A 40-member 2-km storm-scale ensemble is downscaled from the mesoscale ensemble analyses at 0000 UTC 22 May 2011 in a one-way nested configuration. The domain is centered on Ada and covers most of Oklahoma and the northern part of Texas with $203 \times 163 \times 51$ grid points (Fig. 2c). To introduce smaller-scale perturbations into the convective-scale ensemble, samples from a Gaussian distribution with zero mean are drawn at each grid point in the domain. Then, a two-dimensional recursive filter (Jung et al. 2012) with a decorrelation length scale of 6 km is applied to these

TABLE 3. List of experiments conducted and the number of volume scans of radar observations assimilated during the 45-min DA period from 0030 through 0115 UTC 22 May 2011.

Expt	WSR-88D	PAR	PAR-reducedtilts
Tilts (elevation angle, in °) in a complete volume scan	0.46, 0.88, 11.25, 1.75, 2.35, 3.08, 3.98, 5.11, 6.35, 7.97, 10.00, 12.46, 15.57, and 19.45	0.50, 0.90, 1.30, 1.80, 2.40, 3.10, 4.00, 5.10, 6.40, 8.00, 10.00, 12.50, 15.60, and 19.50	0.50, 0.90, 1.30, 1.80, 2.40, 3.10, 4.00, 5.10, 6.40, 8.00, 10.00, 12.50, 15.60, and 19.50
Total No. of volume scans in 15-min DA period (valid 0030–0045 UTC)	5	17 (missing observations at 0045, 0046, and 0047 UTC)	4 (missing observations at 0045, 0046, and 0047 UTC)
Total No. of volume scans in 30-min DA period (valid 0030–0100 UTC)	8	26 (missing observations at 0045, 0046, 0047, 0048, 0049, 0051, 0053, 0054, and 0055 UTC)	6 (missing observations at 0045, 0046, 0047, 0048, 0049, 0051, 0053, 0054, and 0055 UTC)
Total No. of volume scans in 45-min assimilation period (valid 0030–0115 UTC)	12	38 (missing observations at 0045, 0046, 0047, 0048, 0049, 0051, 0053, 0054, 0055 0103, 0107, and 0108 UTC)	10 (missing observations at 0045, 0046, 0047, 0048, 0049, 0051, 0053, 0054, 0055 0103, 0107, and 0108 UTC)

a) Mesoscale Domain

b) Mesoscale Data Assimilation Experiment Timeline

c) Storm-scale Domain

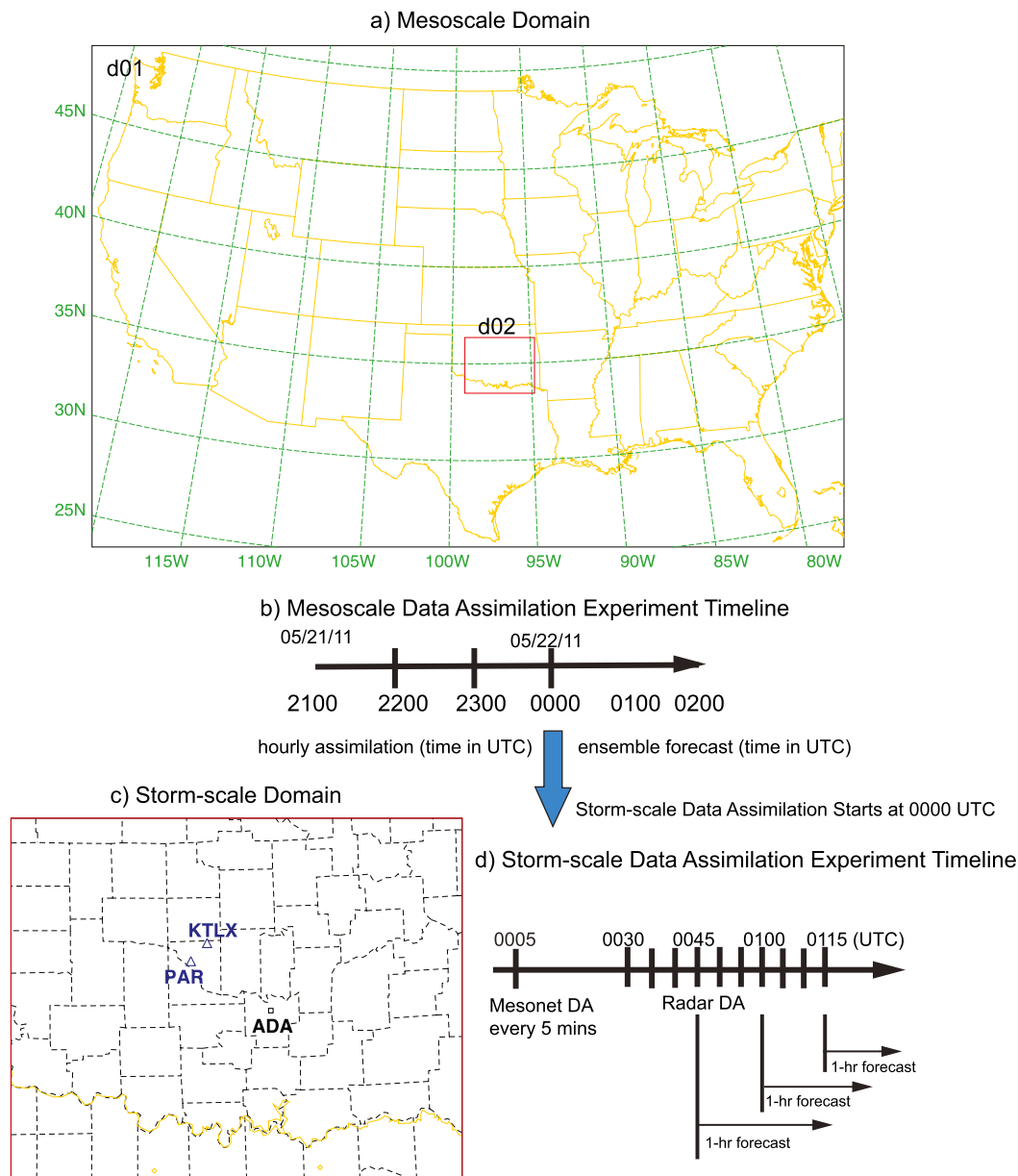d) Storm-scale Data Assimilation Experiment Timeline

FIG. 2. (a) The mesoscale domain (d01) covering the CONUS and the nested storm-scale domain (d02). (b) The timeline of the mesoscale DA experiments. (c) The storm-scale domain with county borders (d02, enlarged) and locations of WSR-88D (KTLX, blue triangle), PAR (blue triangle), and Ada (black square). (d) The timeline of the storm-scale DA and forecast experiments.

samples horizontally, and a homogeneous Gaussian filter with a decorrelation length scale of 4 km is applied vertically. This generates smoothed, spatially correlated perturbations, and these are added to the interpolated mesoscale ensemble at 0000 UTC. The smoothed perturbations have zero mean and standard deviations of $2\,\mathrm{m\,s}^{-1}$ for the horizontal velocity components u and v and $1\,\mathrm{K}$ for potential temperature θ over the entire domain. The perturbation standard deviations of the mixing ratios for water vapor q_v, cloud water q_c, rainwater q_r, ice q_i, snow q_s, hail q_h, and graupel q_g are set to 10% of their values at each grid point where the observed reflectivity is larger than 10 dBZ. Only positive perturbations are retained for θ, q_v, q_c, q_r, q_i, q_s, q_h, and q_g. The effect of the recursive filter is similar to but computationally more efficient than that used by Tong and Xue (2008).

Oklahoma Mesonet (Brock et al. 1995; McPherson et al. 2007) observations (i.e., 10-m u, v; 2-m temperature

T; and relative humidity r_h) are assimilated every 5 min into the storm-scale ensemble starting from 0005 UTC and ending at 0020 UTC using 3D EnSRF (Fig. 2d) DA. A cutoff radius of 50 km is used in the horizontal and 6 km in the vertical for covariance localization [as in Snook et al. (2015), similar to Sobash and Stensrud (2015)]. A 15% multiplicative inflation factor and relaxation-to-prior spread (RTPS; Whitaker and Hamill 2012) with a relaxation factor of 0.85 are applied over the whole domain to all model variables to help maintain ensemble spread during the period of mesonet data assimilation. These values are selected based on several sensitivity studies (not shown).

The radar reflectivity and radial velocity observations from the WSR-88D or PAR are assimilated into the storm-scale ensemble starting at 0030 UTC using the 4DEnSRF (Fig. 2d), and the assimilation continues until 0115 UTC with a 5-min assimilation window. To show the effect of the radar data assimilation without the effect of other observation types, Oklahoma Mesonet data are not assimilated during this period.

Both the PAR and WSR-88D radar observation times are reassigned into 1-min batches, as in a traditional EnSRF approach. For example, a ~50-s complete volume scan of PAR observations is reassigned to the nearest minute and the ~4.2-min volume scan WSR-88D observations, which consist of 14 elevation angles, are separated into single-elevation angles and regrouped at 1-min intervals based on the times of the tilts. Therefore, these 1-min data batches contain between two and three tilts for WSR-88D observations rather than full volume scans that are often treated as being collected simultaneously in 3D EnSRF (S. Wang et al. 2013; Yussouf and Stensrud 2010). The 4DEnSRF scheme precalculates the observation prior $H(x)$ for all these observations every 1 min to perform an analysis every 5 min (S. Wang et al. 2013). Specifically, to produce an analysis valid at time t, the 4DEnSRF uses five batches of data and their priors at $t - 2$ min, $t - 1$ min, t, $t + 1$ min, and $t + 2$ min, with each batch consisting of observations within 30 s of the batch time.

The standard deviations of the WSR-88D reflectivity and radial velocity observation errors are assumed to be 5 dBZ and 3 m s^{-1}, respectively, following Putnam et al. (2014). After several sensitivity experiments, the same observation error standard deviations as those for the WSR-88D dataset are used for the PAR dataset as well. The cutoff radius used in covariance localization for the storm-scale ensemble is 6 km in both the horizontal and vertical, the same as those used in Jung et al. (2012), while the time localization is assumed to be 5 min, following S. Wang et al. (2013). To help maintain ensemble spread, RTPS with a relaxation factor of 0.9 is applied

over the entire region, and multiplicative inflation of 20% is applied to the prior ensemble in regions directly influenced by the radar data during the period of radar data assimilation. These values are selected based on several sensitivity studies and the guidance of earlier studies.

Three DA and forecast experiments are conducted (Table 3) on the 2-km grid, forced by the same mesoscale ensemble at the lateral boundaries. The first experiment assimilates the KTLX WSR-88D radar observations only (referred to as the WSR-88D experiment hereafter), while the second experiment assimilates the full-volume PAR observations (referred to as the PAR experiment hereafter). The third experiment assimilates PAR observations but uses only those tilts that closely match the times of the tilts of the WSR-88D observations (referred to as the PAR-reducedtilts experiment hereafter). Four to five volume scans of PAR observations are needed to reproduce one volume scan of PAR-reducedtilts observations that has the same temporal frequency as in WSR-88D. An example radar observation dataset that is assimilated in the WSR-88D, PAR, and PAR-reducedtilts experiments during a 5-min DA window is shown in Table 4. As mentioned earlier, while the PAR observations have higher temporal resolution than the WSR-88D observations, the PAR observations have a slightly coarser spatial resolution than the WSR-88D observations. Therefore, while experiments WSR-88D and PAR-reducedtilts have similar temporal resolutions, the latter has a coarser spatial resolution. The differences between the PAR and PAR-reducedtilts results will reveal the impact of the higher temporal frequency of the PAR observations. Additional information regarding the experiments is found in Table 2. Finally, 1-h deterministic forecasts are initialized from the ensemble mean analyses and three sets of 1-h ensemble forecasts are initialized from the ensemble analyses for all three experiments after 15-, 30-, and 45-min of ensemble radar DA (Fig. 2d). The analyses and forecasts are used to investigate how quickly and accurately the rapid-scan PAR observations initialize and forecast the storm.

4. Results and discussions

a. Innovation statistics during the DA period

The three DA and forecast experiments assimilate radar observations from two different radar platforms (i.e., the WSR-88D and PAR). To evaluate the performance of the ensemble filter during the 45-min assimilation period, the root-mean-square innovation (RMSI), mean innovation, total ensemble spread (TES), and consistency ratio statistics are calculated in observation

TABLE 4. An example list of tilts of PAR observations that are assimilated in the PAR-reducedtilts experiment. Listed are the tilts and corresponding times of observation used in the WSR-88D, PAR, and PAR-reducedtilts experiments from 0028 to 0031 UTC.

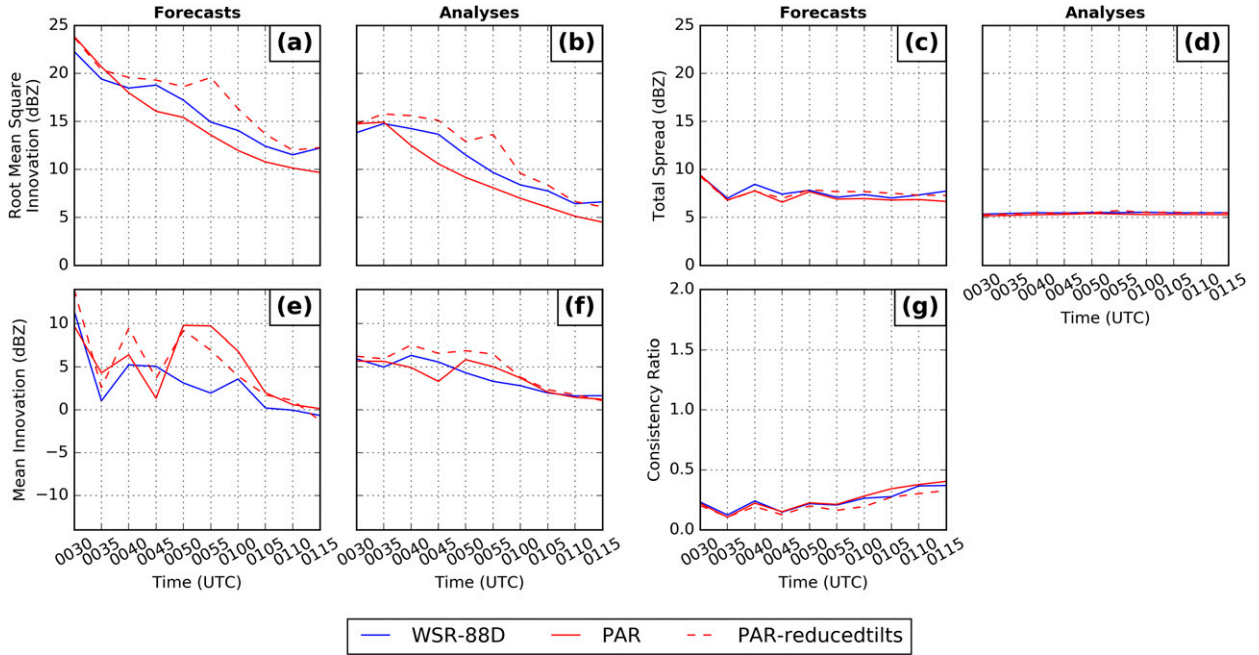| Time (UTC)	WSR-88D expt time [UTC (tilt, in °)]	PAR expt time [UTC (tilt, in °)]	PAR-reducedtilts exp time [UTC (tilt, in °)]
0028	0027:34 (0.5)	0027:37 (0.51)	0027:37 (0.51)
	0028:07 (0.9)	0027:44 (0.9)	0027:44 (0.9)
		0027:50 (1.3)	
		0027:55 (1.8)	
		0028:01 (2.4)	
		0028:04 (3.1)	
		0028:07 (4.0)	
		0028:09 (5.1)	
		0028:11 (6.4)	
		0028:12 (8.0)	
		0028:13 (10.0)	
		0028:14 (12.5)	
		0028:15 (15.6)	
		0028:15 (19.5)	
0029		0029:02 (0.51)	
		0029:09 (0.9)	
	0028:39 (1.4)	0029:15 (1.3)	0029:15 (1.3)
	0028:54 (1.8)	0029:20 (1.8)	0029:20 (1.8)
	0029:09 (2.4)	0029:26 (2.4)	0029:26 (2.4)
	0029:23 (3.0)	0029:29 (3.1)	0029:29 (3.1)
		0029:32 (4.0)	
		0029:34 (5.1)	
		0029:36 (6.4)	
		0029:37 (8.0)	
		0029:38 (10.0)	
		0029:39 (12.5)	
		0029:40 (15.6)	
		0029:40 (19.5)	
0030		002945 (0.51)	
		0029:51 (0.9)	
		0029:57 (1.3)	
		0030:03 (1.8)	
		0030:08 (2.4)	
		0030:12 (3.1)	
	0029:38 (4.0)	0030:15 (4.0)	0030:15 (4.0)
	0029:52 (5.0)	0030:17 (5.1)	0030:17 (5.1)
	0030:05 (6.3)	0030:19 (6.4)	0030:19 (6.4)
	0030:19 (8.0)	0030:21 (8.0)	0030:21 (8.0)
		0030:22 (10.0)	
		0030:23 (12.5)	
		0030:23 (15.6)	
		0030:24 (19.5)	
0031		0030:30 (0.51)	
		0030:37 (0.9)	
		0030:44 (1.3)	
		0030:50 (1.8)	
		0030:56 (2.4)	
		0031:01 (3.1)	
		0031:05 (4.0)	
		0031:09 (5.1)	
		0031:12 (6.4)	
		0031:15 (8.0)	
	0030:33 (10.2)	0031:17 (10.0)	0031:17 (10.0)
	0030:46 (12.4)	0031:18 (12.5)	0031:18 (12.5)
	0031:00 (15.6)	0031:20 (15.6)	0031:20 (15.6)
	0031:14 (19.7)	0031:21 (19.5)	0031:21 (19.5)

FIG. 3. Observation-space diagnostic statistics. (a) Forecast and (b) analysis RMSI. (c),(d) As in (a),(b), but for TES. (e),(f) As in (a),(b), but for mean innovation (positive values denote that the observations are larger than the ensemble mean). (g) Forecast consistency ratio for reflectivity (dBZ) from the three data assimilation and forecast experiments. Calculations are limited to locations where observed and/or ensemble mean reflectivity exceeds 15 dBZ.

space against the observations that each experiment assimilated and are shown in Fig. 3. The statistics are calculated at the time of the observations and only at locations where the observed or model reflectivity is greater than 15 dBZ. The RMSI is calculated using the following equation (Dowell and Wicker 2009):

$$\text{RMSI} = \sqrt{\langle(d - \langle d \rangle)^2\rangle} \quad \text{and} \quad (1)$$

$$d = y^0 - \overline{H(\mathbf{x}^f)} \quad \text{or} \quad d = y^0 - \overline{H(\mathbf{x}^a)}, \quad (2)$$

and the brackets indicate an average over all observations in a radar volume. Here, y^0 is the observation; H is the observation operator, which maps the model state to the observation type and location; $\mathbf{x}$ represents the model state vector; the superscript f indicates a prior estimate (i.e., before the observation is assimilated); and the superscript a indicates a posterior estimate (i.e., after the observation is assimilated). The TES is defined in terms of the observation prior as

$$\text{TES} = \sqrt{\sigma^2 + \left\langle \frac{1}{N-1} \sum_{n=1}^{N} \left[H(\mathbf{x}_n) - \overline{H(\mathbf{x})}\right]^2 \right\rangle}, \quad (3)$$

where N is the number of ensemble members (40 in our experiment), n is an index that identifies a particular ensemble member, and the observation error standard deviation σ is assumed to be 5.0 dB for both WSR-88D and PAR reflectivity observations, as mentioned earlier. Finally, the consistency ratio is defined as in Dowell and Wicker (2009):

$$\text{consistency ratio} = \left(\frac{\text{TES}}{\text{RMSI}}\right)^2$$

$$= \frac{\sigma^2 + \left\langle \frac{1}{N-1} \sum_{n=1}^{N} \left[H(\mathbf{x}_n^f) - \overline{H(\mathbf{x}^f)}\right]^2 \right\rangle}{\langle(d - \langle d \rangle)^2\rangle}. \quad (4)$$

All three experiments start with an analysis RMSI of ~15 dBZ (Fig. 3b); by the end of the assimilation period, the analysis RMSI is reduced to ~5–7 dBZ. The forecast and analysis RMSI values from the PAR experiment are generally less than those from the other experiments. Additionally, the effect of the missing PAR volumes between 0045 and 0055 UTC (see Table 3) is apparent in the increased RMSI near 0055 UTC in both the analyses and forecasts in the PAR-reducedtilts experiment. However, by the 0115 UTC cycle, the RMSI is stabilized (Fig. 3a), which suggests that the missing PAR observations have minimal effect by the end of the assimilation period.

Furthermore, the TES (Figs. 3c,d) is similar for all experiments in either the forecasts or the analyses,

suggesting the ensembles are fairly configured. The consistency ratios are also comparable in magnitude between the experiments, with values between 0.1 and 0.4 (Fig. 3g). These values are well below 1, suggesting underdisperson in the ensemble, which is commonly seen in storm-scale real-data ensemble DA studies (e.g., Jung et al. 2012; Yussouf et al. 2013, and references therein). Despite the spread deficiency, the filter shows no sign of divergence during the 1-h assimilation period, indicating the reasonable robustness of the DA system.

The mean innovation (Figs. 3e,f) is largely positive, indicating that the model reflectivity is lower than the observed reflectivity. The underprediction of reflectivity in the model during the assimilation period is also seen in other studies (Dawson et al. 2012; Yussouf et al. 2015). As expected, the forecast and analysis mean innovation results generally decrease with time as more data are assimilated. There are some apparent oscillations in the forecast mean innovation in the early part of the assimilation period that are the result of the overprediction of spurious echoes and the underprediction of the geographical extent of storms before the forecast is sufficiently improved. The intensity of the storms is underpredicted at 0035 UTC, while the spatial coverage of the reflectivity is overpredicted, leading to a small mean innovation. Radar DA at this time is too aggressive at removing reflectivity, resulting in a large positive mean innovation and large RMSI at 0040 UTC. Both spurious echoes and the underprediction of storm intensity are improved at 0045 UTC, as more data are assimilated at 0040 UTC, leading to a smaller mean innovation. The main reason for the large positive mean innovation at 0050 UTC is different. As mentioned earlier, the PAR scan sector shifts approximately $21°$ counterclockwise at 0050 UTC, meaning the PAR is observing storms that were previously not in the PAR coverage area. Those storms have yet to spin up in the model, leading to underprediction and a large positive mean innovation (Figs. 3e,f) during the 0050 UTC assimilation. After 0055 UTC, both mean innovation and RMSI continue to decrease, indicating that the filter is stable.

b. Analyzed near-surface cold pool and vertical vorticity

Studies by Dawson et al. (2010) and Putnam et al. (2014) have shown the importance of the analyzed and predicted cold pool in convective storms on their dynamics and evolution. To evaluate the analyzed cold pools and associated low-level mesocyclones, the ensemble mean analyses of equivalent potential temperature θ_e, horizontal winds, and vertical vorticity at the first model level or about 25 m above ground from the three

experiments after 15 (valid 0045 UTC), 30 (valid 0100 UTC), and 45 min (valid 0115 UTC) of DA cycles are shown in Fig. 4.

After 15 min of DA, the cold pool in storm B in the PAR experiment is the coldest out of all three experiments (minimum θ_e of 319 K in Fig. 4d). Assimilating more reflectivity observations in the PAR experiment leads to a stronger cold pool, likely because of the negative correlation between reflectivity and temperature in the cold pool (Dowell et al. 2011). The low-level mesocyclones are also relatively weak in all experiments, though the WSR-88D experiment has the strongest examples ($1.9 \times 10^{-3}\,\text{s}^{-1}$), followed by the PAR experiment ($1.7 \times 10^{-3}\,\text{s}^{-1}$), and then by the PAR-reducedtilts experiment ($1.4 \times 10^{-3}\,\text{s}^{-1}$). As 4DEnSRF uses a 5-min assimilation window, the missing PAR observations during the last assimilation cycle from the initial 15 min of the DA period (Table 3) directly impact the analysis and may be partly responsible for weaker low-level mesocyclone PAR-reducedtilts.

After 30 min of DA, the PAR (Fig. 4e) experiment has stronger cold pools than the other two experiments, in general, in storm A and storm B. Additionally, the PAR experiment has the strongest low-level mesocyclone for both storms A and B. The peak of $5.4 \times 10^{-3}\,\text{s}^{-1}$ is in storm A. By this time, 8, 26, and 6 volume scans of observations are assimilated into the WSR-88D, PAR, and PAR-reducedtilts experiments, respectively (Table 3), leading to the weakest mesocyclone being found in the PAR-reducedtilts experiment.

After an additional 15-min of DA (valid 0115 UTC), the PAR experiment continues to have the strongest vorticity values associated with storm B, with the maximum vertical vorticity reaching $6.6 \times 10^{-3}\,\text{s}^{-1}$ (Fig. 4f) while the other two experiments produce much smaller maximum values (Figs. 4c,i). In addition, the minimum θ_e for both the WSR-88D and PAR experiments are in the cold pool for storm A; the minimum θ_e values are similar between these two experiments. For storm B, the cold pool has approximately the same minimum θ_e in all three experiments. However, approximating the outline of the cold pool as the 336-K contour, the PAR experiment has a slightly more widespread cold pool.

c. Analyses and forecasts of reflectivity

To evaluate the impacts of DA on the forecasts, the observed National Mosaic and Multi-Sensor QPE (NMQ) 3D radar reflectivity mosaic product (Zhang et al. 2011) reflectivity is compared with the analyses and 15-min forecasts from the ensemble member closest to the mean (Figs. 5 and 6). This member is chosen in a similar way to that in Yussouf et al. (2013). It is defined as the member with the smallest normalized
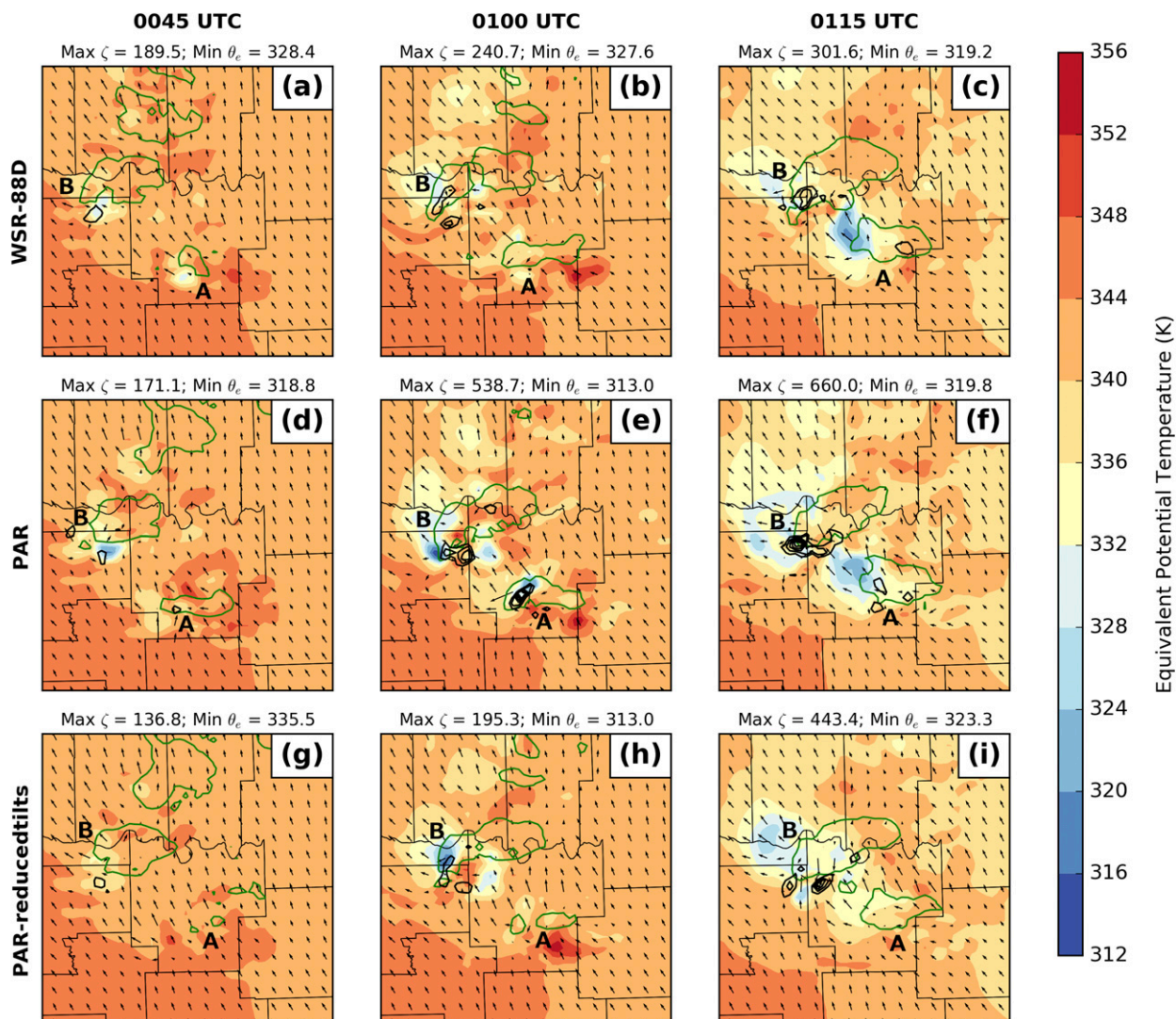
FIG. 4. The ensemble mean analyses of vertical vorticity (black contours at intervals of $100 \times 10^{-5}\,\mathrm{s}^{-1}$; maximum vorticity is shown in each panel with unit $\times 10^{-5}\,\mathrm{s}^{-1}$), horizontal wind vectors and θ_e (colored; in 4-K increments; minimum is shown in each panel) after 15 (valid 0045 UTC), 30 (valid 0100 UTC), and 45 (valid 0115 UTC) min of DA from (a)–(c) WSR-88D, (d)–(f) PAR, and (g)–(i) PAR-reducedtilts experiments at the first model grid level (∼25 m) above ground. Green contours represent 35-dBZ reflectivity analyses.

root-mean-square difference from the mean in potential temperature and u and v wind components. The reflectivity analyses at 2 km MSL valid at 0045 UTC (after 15 min of DA or three assimilation cycles) are able to capture both storms A and B in all three experiments, though storm A in particular has lower reflectivity in the analyses than the observations (Figs. 5a,d,g,j). Because the PAR does not observe the cells to the north of storm B until 0050 UTC, they are not well represented at this time in the PAR and PAR-reducedtilts experiments (Figs. 5g,j). In particular, both experiments have one intense storm instead of two weaker storms.

As PAR observations of the two cells to the north of storm B start when the scan sector changes at 0050 UTC,

the reduction in intensity of these cells induced by the PAR observations is apparent in the PAR experiment at 0100 UTC (Fig. 5h). While seven full volumes are assimilated in the PAR experiment, only two partial volumes are assimilated in the PAR-reducedtilts experiment because of the missing data discussed earlier. As a result, those storms are still poorly resolved at 0100 UTC (Fig. 5k). Otherwise, only minor structural differences are evident between the experiments. By the 0115 UTC analyses, all three experiments show similar storm structures, suggesting sufficient observations are assimilated by this time (Figs. 5f,i,l).

The 15-min forecast from the member closest to the ensemble mean is examined in Fig. 6. In the forecasts
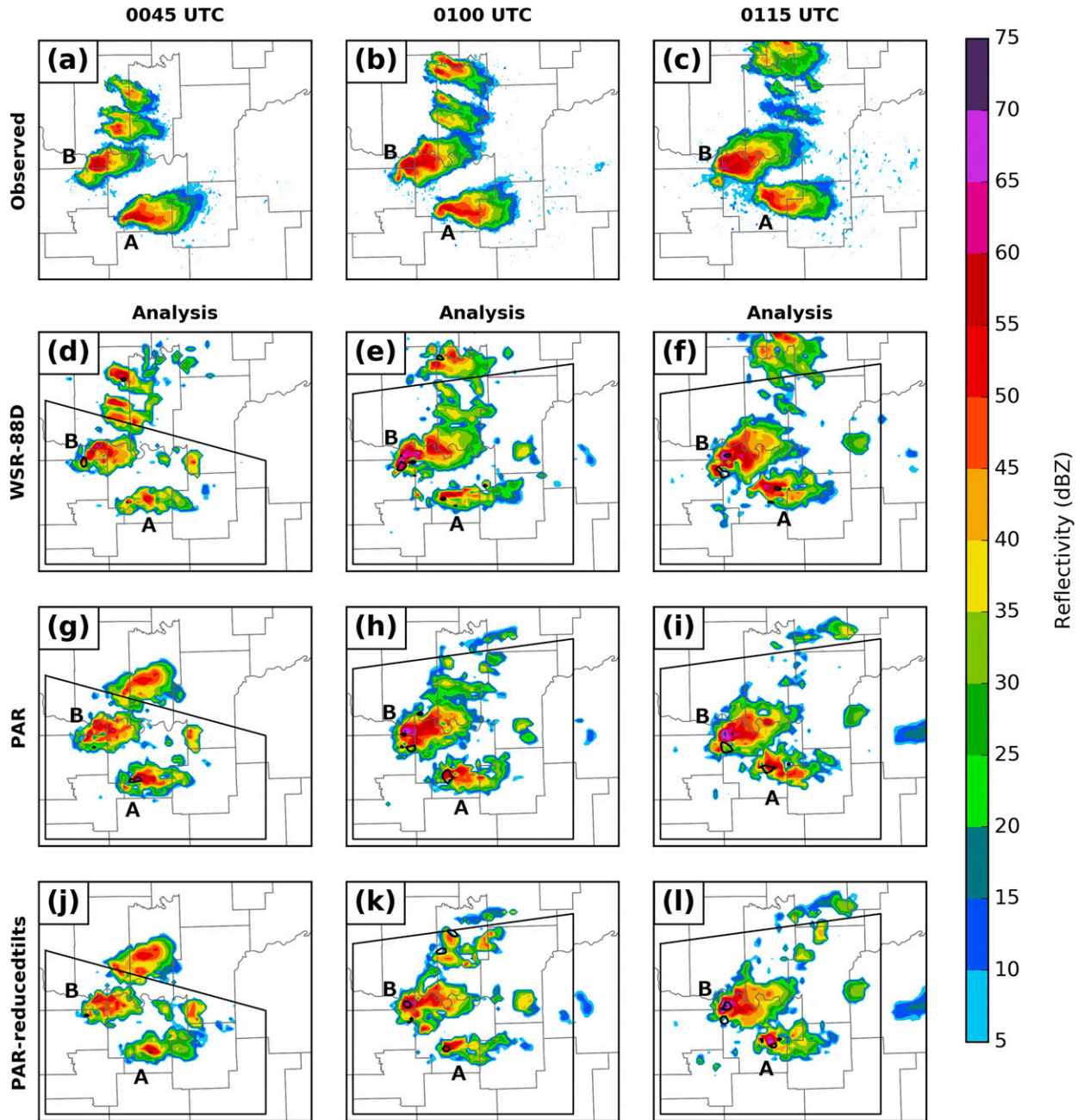
FIG. 5. (a)–(c) The NMQ reflectivity observations (colored, in 5-dB*Z* increments) and analyses from the member closest to the mean at (left) 0045, (center) 0100, and (right) 0115 UTC from the (d)–(f) WSR-88D, (g)–(i) PAR, and (j)–(l) PAR-reducedtilts experiments. Reflectivity at 2 km AGL is color filled. The $0.004\,\mathrm{s}^{-1}$ vertical vorticity contours are given in solid black. The verification domain for the skill scores in Figs. 8 and 9 are shown by the black box. The portion of the domain shown here is over southeast OK.

initialized at 0045 UTC, the intensity and structure of storm A in the PAR experiment matches the observations more closely (Figs. 6a,d,g,j). However, storm B, which is located near the boundary of the PAR coverage area, is merging with a spurious supercell outside of the PAR coverage area. In the forecasts initialized at

0100 UTC, the overall structure of storm B in the WSR-88D and PAR-reduced tilts experiments is more realistic than the corresponding initialization (see Figs. 5e,k). Additionally, the ensemble member closest to the mean happens to develop much less spurious cells to the east of storms A and B in the PAR and PAR-reducedtilts
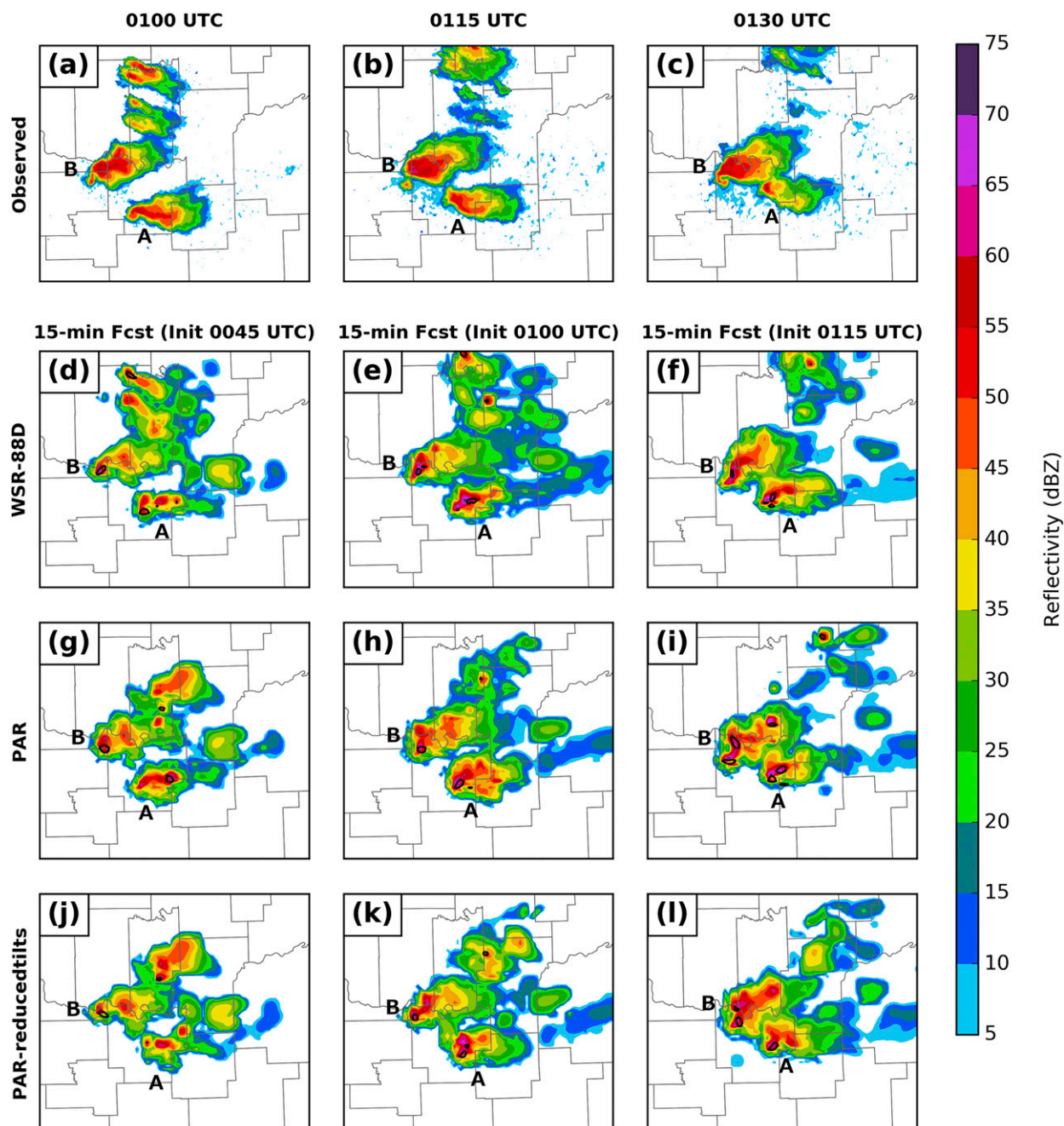
FIG. 6. As in Fig. 5, but for 15-min deterministic forecasts initialized from the ensemble member closest to the mean. Note that the verification domain for the skill scores is omitted.

experiments compared with the WSR-88D experiment. All other ensemble members (not shown) show similar results, and this is consistent with our observation that northern storms outside of the PAR coverage area are underpredicted in the PAR and PAR-reducedtilts experiments, producing less convection.

Additionally, the reflectivity in storm A is much more intense in all three experiments than in the observations,

and the simulated storms continue to display hook echoes, whereas the observed storm does not. In fact, storm A does not dissipate through the end of the 1-h forecast in any of the experiments (not shown). Thus, the reflectivity forecasts from 15 min through the end of the run are considered poor. Furthermore, the 15-min forecasts initialized at 0115 UTC (Figs. 6f,i,l) are largely similar, except that the PAR experiment and, to a lesser

extent, the PAR-reducedtilts experiment develop a spurious vorticity maximum in the northeastern quadrant of storm B. Also, storm A in the 0115 UTC forecasts is still much stronger than was observed, though it does begin to dissipate near the end of the run.

One problem seen in all three experiments is the faster propagation of supercells to the north and east compared with the observations. Similar problems have been seen in many prior storm-scale radar DA studies (e.g., Dawson et al. 2012, 2015; Xue et al. 2014; Yussouf et al. 2015, 2016; Stensrud and Gao 2010, to name a few). Stensrud and Gao (2010) suggest that this may be because the model is unable to develop midlevel pressure perturbations that lead to deviant motion in supercells. Xue et al. (2014) speculate that this may be due to errors in analyzing the storm environment, which leads to incorrect steering winds in the model. Fiori et al. (2010) found that the storm motion depends on the turbulence closure model and grid spacing. Reducing errors associated with supercell motion in storm-scale NWP is worthy of further investigation, however addressing it is beyond the scope of this paper.

d. Forecast probability of low-level vorticity

The 2-km model horizontal grid spacing used in this study is far too coarse to explicitly resolve tornadoes and is barely capable of resolving mesocyclone-scale features of the supercell. To infer the amount of low-level rotation from the three experiments, the ensemble forecast probability of low-level vorticity is compared with the surface–2 km MSL mesocyclone circulations generated by the Warning Decision Support System–Integrated Information (WDSS-II; Lakshmanan et al. 2007) (Miller et al. 2013) from KTLX radar observations (Stensrud and Gao 2010; Dawson et al. 2012; Yussouf et al. 2013, 2015; Xu et al. 2015). The vorticity probabilities are calculated at the first model level above ground level ($\sim$25 m AGL) during the 0–1-h forecast period. The forecast output (which is written out at 5-min intervals) from each ensemble member initialized from a certain analyses time is checked to see whether the vorticity exceeds a threshold value within a radius of 4 km in the horizontal direction around each horizontal grid point at any output time during the 1-h forecast period, and the vorticity probabilities are calculated from the number of members exceeding the threshold values. A threshold of $0.0015\,\mathrm{s}^{-1}$ is used for vertical vorticity. The 1-h forecast probability of vorticity is examined every 15 min from after 15, 30, and 45 min (valid 0045, 0100, and 0115 UTC initialization times) of radar DA and is compared with the WDSS-II rotation track (Fig. 7).

The 1-h forecast probability of low-level vorticity exceeding $0.0015\,\mathrm{s}^{-1}$ initialized at 0045 UTC shows largely low (<40%) probabilities of vorticity (Figs. 7a,d,g). The PAR experiment (Fig. 7d) has the largest overlap between the forecast vorticity swath and the WDSS-II rotation track. The WSR-88D experiment (Fig. 7a) shows the highest probability values ($\sim$50%) displaced well to the north and west of the WDSS-II track, and the PAR-reducedtilts experiment shows only weak probabilities overlapping the WDSS-II track.

The forecast probabilities of strong low-level rotation increase with an additional 15 min of DA (Figs. 7b,e,h), and the forecast vorticity swaths are aligned better with the observed WDSS-II track compared with the 0045 UTC forecasts. The WSR-88D experiment (Fig. 7b) has very low probability over the beginning part of the observed strong rotation track but increases to high probabilities over the later part of the track. The PAR-reducedtilts experiment (Fig. 7h) has coverage of midrange probabilities (40%–60%) over the first part of the track, but the probabilities never increase above $\sim$60%. On the other hand, the PAR experiment (Fig. 7e) has coverage of high probabilities over the first part of the observed rotation track and at least midrange probabilities over the rest of the track. Thus, the assimilation of the higher temporal frequency PAR observations clearly produces more reasonable probabilistic forecasts of vorticity with only 30 min of DA compared to the assimilation of WSR-88D data.

The forecast of low-level vorticity initialized after 45 min of DA generates relatively large areas with probability > 90% in all three experiments (Figs. 7c,f,i). These areas are displaced slightly south of the WDSS-II track in all experiments. As in the forecasts initialized at 0115 UTC, the PAR experiment (Fig. 7f) has better coverage in the early part of the track as compared to the WSR-88D and PAR-reducedtilts experiments (Figs. 7c,i). Additionally, the spurious vorticity maximum seen in the 2 km MSL vorticity from the PAR and PAR-reduced tilts experiments (see Figs. 6i,l) does not extend down to the surface. However, aside from the coverage in the early part of the rotation track, few differences are apparent between experiments in the forecasts initialized at 0115 UTC.

Though the above analysis has primarily focused on storm B, the forecasts for storm A show similar results. In particular, in the forecasts initialized at 0100 UTC, the PAR experiment shows higher probabilities of vorticity for storm A than the WSR-88D and PAR-reducedtilts in the early part of the swath, where there is observed rotation from the WDSS-II track. Additionally, the probabilities of vorticity for storm A increase with eastward extent in the WSR-88D and PAR-reducedtilts
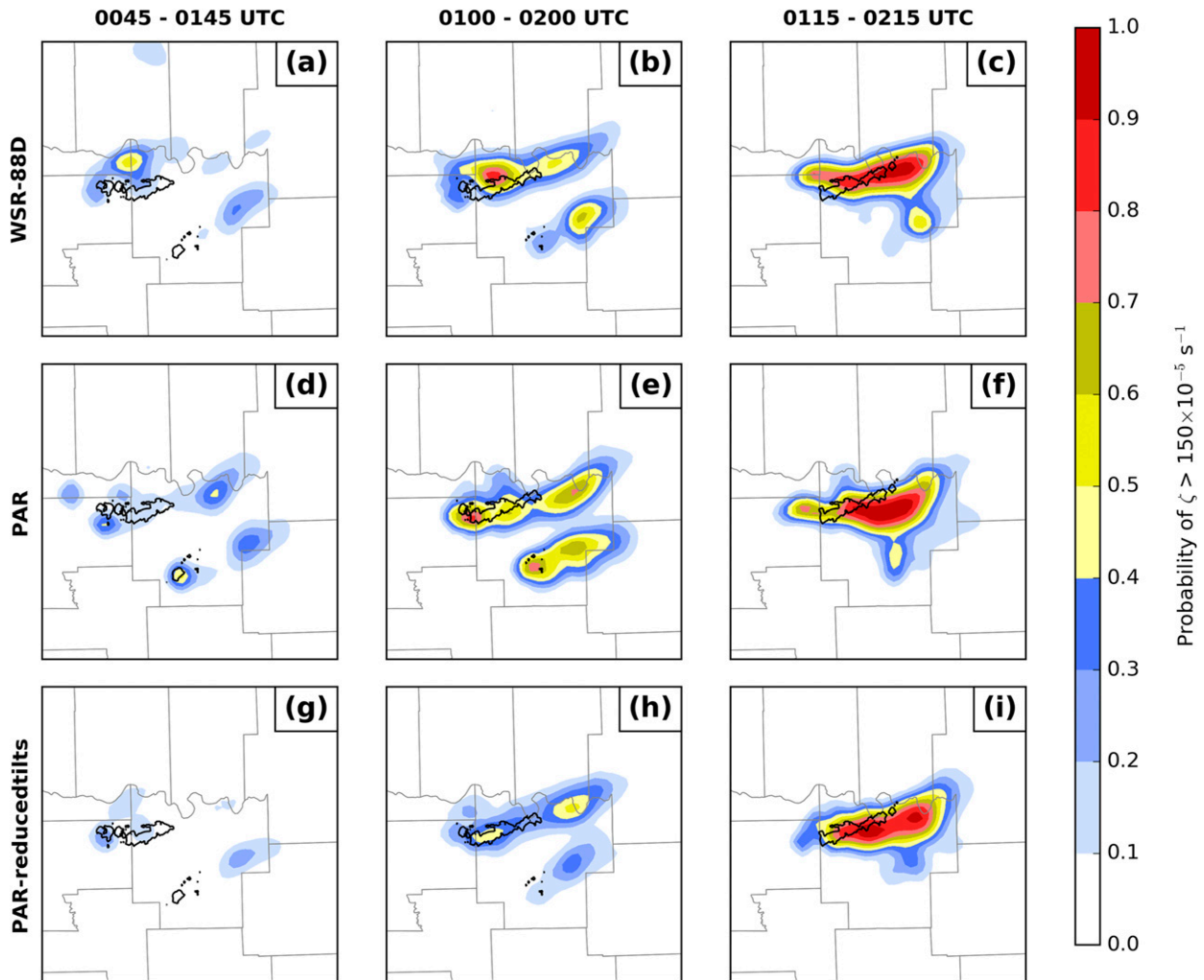
0045 - 0145 UTC **0100 - 0200 UTC** **0115 - 0215 UTC**

FIG. 7. The 1-h forecast neighborhood ensemble probability of vertical vorticity exceeding a threshold of $0.0015 \, \mathrm{s}^{-1}$ at the first model level above ground from (a)–(c) WSR-88D, (d)–(f) PAR, and (g)–(i) PAR-reducedtilts experiments initialized after (left) 15 min (valid 0045 UTC), (center) 30 min (valid 0100 UTC), and (right) 45 min (valid 0115 UTC) of DA. The black contours overlaid are the WDSS-II-generated KTLX low-level mesocyclone rotation exceeding $0.01 \, \mathrm{s}^{-1}$ vorticity during the 0–1-h forecast periods.

experiments, which is not reflected in the WDSS-II rotation track. In contrast, the vorticity probabilities in the PAR experiment remain approximately the same with a slight reduction in value with eastward extent. This is consistent with storm A being underpredicted during early DA cycles in the WSR-88D and PAR-reducedtilts experiments and dissipating much later than the observations. However, the PAR experiment was able to retrieve the intensity and the spatial coverage much better during early cycles although dissipation was delayed as in the other two experiments.

e. Skill scores of ensemble reflectivity forecasts

To quantify the accuracy of reflectivity forecasts from the 40-member ensembles during the 1-h forecast

period, the equitable threat scores (ETSs; Wilks 2006) are calculated from the three experiments for reflectivity exceeding thresholds of 25 and 40 dBZ (Fig. 8) using the NMQ reflectivity observations. These thresholds are chosen to focus on light precipitation areas and heavy convective cores, respectively. Ensemble members are aggregated by summing the number of hits, misses, and false alarms from each ensemble member in the ETS calculation. That is,

$$\mathrm{ETS} = \frac{\overline{h} - h_r}{\overline{h} + \overline{m} + \overline{f} - h_r}; \quad h_r = \frac{(\overline{h} + \overline{m})(\overline{h} + \overline{f})}{\overline{n}}, \quad (5)$$

where $\overline{h} = \sum_i h_i$ and h_i is the number of hits in ensemble member i. The quantities $\overline{m}$, $\overline{f}$, and $\overline{n}$ are misses, false
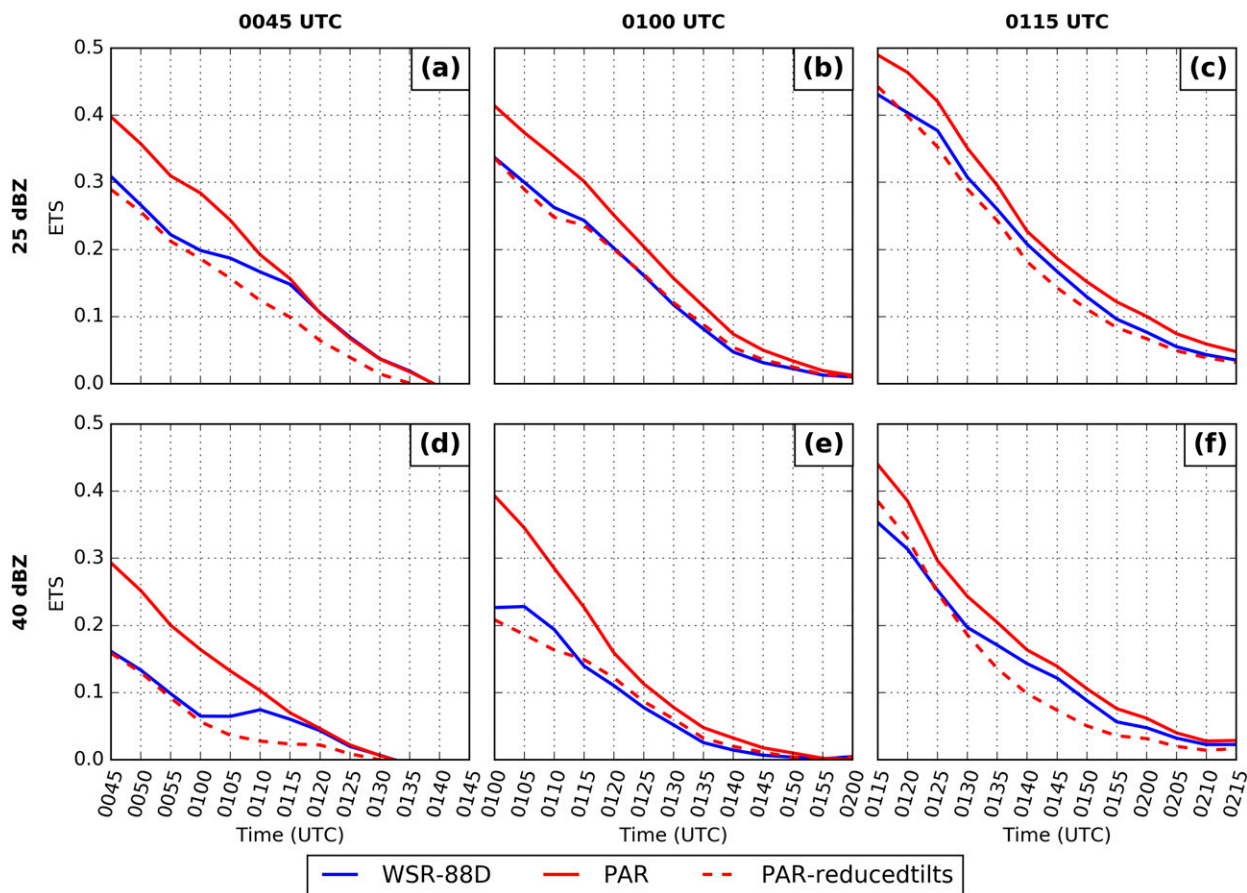
FIG. 8. ETSs vs forecast times (UTC) for reflectivity thresholds of (top) 25 and (bottom) 40 dBZ from the three experiments. Forecasts are initialized after (a),(d) 15 min (valid 0045 UTC), (b),(e) 30 min (valid 0100 UTC), and (c),(f) 45 min (valid 0115 UTC) of DA. Calculations are performed over a small subdomain (see text for details).

alarms, and the total number of grid points, respectively, and are defined in a similar manner to the hits. This is similar, though not equivalent, to taking the mean of the ETS from the members. An ETS of 0 indicates no skill, while an ETS of 1 indicates a perfect forecast by all ensemble members. To eliminate areas that were not observed by the PAR, which would unfairly penalize that experiment, verification regions were created at the 0045, 0100, and 0115 UTC analysis times (see Fig. 5). Each region is entirely contained within the PAR scan sector at that time. The verification regions were translated during the respective forecasts along with the storms to keep the entirety of the observed and forecast storms in the region. Additionally, the ETS is computed over the entire depth of the storm.

The ETSs are found largely to increase with decreasing forecast lead time as expected in all three experiments, declining to near or below 0 by the end of the forecast periods. In general, the PAR experiment has a higher ETS for both the 25- and 40-dBZ

thresholds than the WSR-88D experiment for the forecasts (Fig. 8) despite the missing observations and lower spatial resolution. We suspect that those limitations are responsible for a similar or slightly higher ETS in the WSR-88D experiment in general compared with the PAR-reducedtilts experiment. The differences between the WSR-88D and PAR experiments are evident only for the first 30 min of the forecasts initialized at 0045 UTC (Figs. 8a,d), while differences are noticeable almost to the end of the 1-h forecast period for forecasts initialized at 0100 and 0115 UTC (Figs. 8b,c,e,f). The ETS of the PAR-reducedtilts experiment remains lower than that of the PAR experiment for the duration of all 1-h forecasts, indicating the benefit of high-temporal-frequency observations.

The area under the relative operating characteristic (ROC; Mason 1982) curve (AUC) is calculated for a range of reflectivity thresholds (10–50 dBZ), and results are shown in Fig. 9 for the analyses and forecasts. As discussed in Snook et al. (2012), ROC
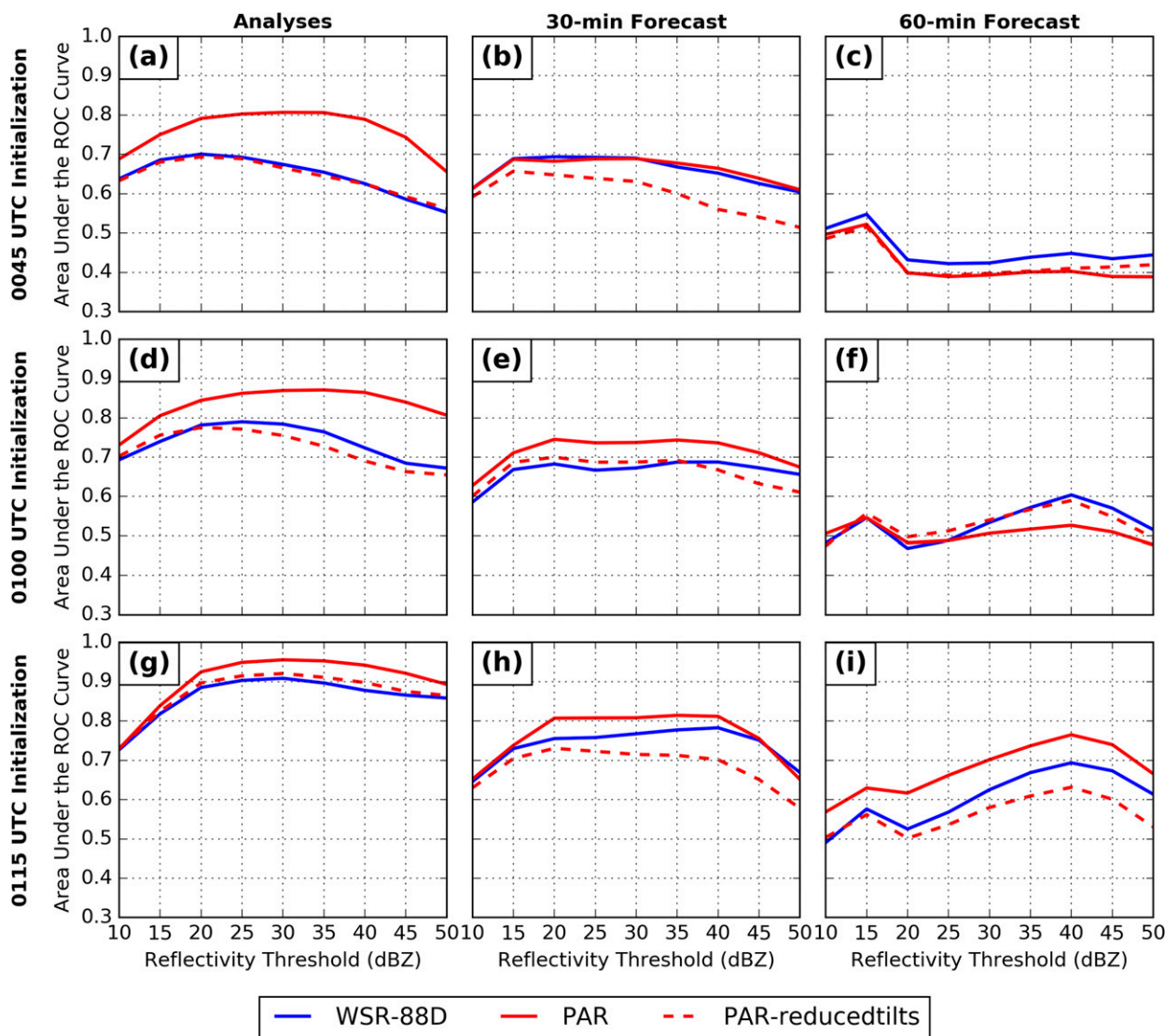
FIG. 9. AUC results from the (left) analyses after 15, 30, and 45 min of DA; (center) 30-min forecasts; and (right) 1-h forecasts for
reflectivity thresholds ranging from 10 to 50 dBZ. Calculations are performed over a small subdomain (see text for details).

measures hit and false alarm rates at varying pro-
bability thresholds (Mason and Graham 1999); it
therefore provides information on the ability of a
probabilistic forecast system to correctly discriminate
between events and nonevents. A forecast with perfect
skill has an AUC of 1.0 and 0.5 means zero skill.

All three experiments have high AUCs in the analyses
(Figs. 9a,d,g) and the value decreases as the forecast
lead times increases (cf. Figs. 9b,e,h and 9c,f,i). The
30-min forecasts after 15 min of DA are just below
the skillful range (AUC > 0.7), and the 60-min fore-
casts have very small AUCs, indicating no ability to
discriminate (AUC < 0.5). The 30-min forecasts after
30 and 45 min of DA increase the AUCs to above 0.7

for most thresholds for the PAR experiment, sug-
gesting that at least eight radar volume scans (~30 min
of DA) are needed to produce operationally useful
forecasts.

The reasons for the improved ETS scores and AUCs
can be seen in Fig. 10, which shows the 10-min forecast
from the 0100 UTC initialization of the number of hits,
misses, and false alarms at the 25-dBZ threshold at each
grid point, summed over all members of the ensemble.
All three experiments have large numbers of hits where
the observed storms overlap with the storms in the en-
semble. The majority of the misses in all three experi-
ments occur to the south and west of storms A and B
(Figs. 10d,e,f), and the majority of false alarms occur to
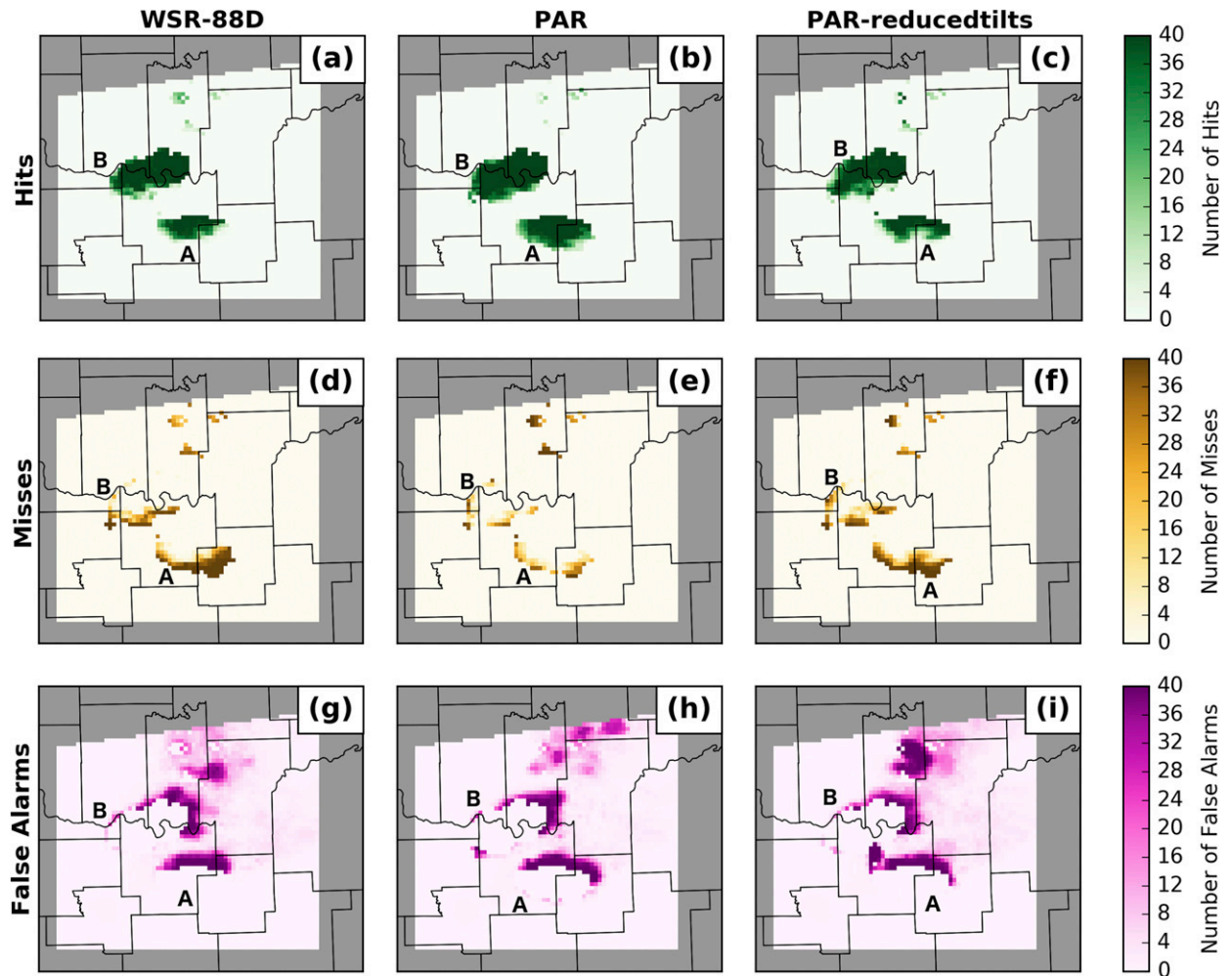
FIG. 10. The 10-min forecast from the 0100 UTC initialization of the number of (top) hits, (middle) misses, and (bottom) false alarms at the 25-dBZ threshold at each grid point, summed over all ensemble members, at 2 km MSL.

the northeast of storms A and B (Figs. 10g,h,i), likely as a result of the faster propagation of storms in the model, as noted earlier. The three experiments are largely similar, except the PAR experiment better captures the southern extent of both storms A and B, resulting in fewer misses and more hits in those regions. This directly increases the ETS score and also results in larger AUCs because of the higher probability of detection, which is used in computing the ROC curve.

Overall, the PAR experiment generates the highest AUCs and the PAR-reducedtilts experiment the lowest AUCs during the 1-h forecast period. In the analyses, these differences are largest after 15 min of DA and decrease as more data are assimilated. However, the largest differences in the 30-min forecasts are after 30 min of DA, and in the 60-min forecasts, the AUCs are largely the same between experiments. These results

suggest that the PAR data are most useful in DA windows that are ~30 min long.

5. Summary and discussions

To evaluate the impact of high-temporal-resolution PAR observations compared with the current operational WSR-88D observations on convective storm prediction, three DA and forecast experiments are conducted for the 22 May 2011 Ada, Oklahoma, tornadic supercell event using radial velocity and reflectivity observations from both rapid-scan NWRT PAR and WSR-88D KTLX. The experiments are conducted with the ARPS model and its 4DEnSRF DA system using a heterogeneous mesoscale environment. The first experiment assimilates traditional WSR-88D radar observations, the second experiment assimilates observations from the NWRT PAR, and the third

experiment assimilates PAR observations with WSR-88D-like temporal frequency (PAR-reducedtilts experiment). The WSR-88D and PAR experiments are designed to compare the accuracy of the forecasts due to two different temporal resolutions from the different radar platforms. The PAR-reducedtilts experiment picks a subset of elevations from the rapid-scan PAR observations from the observation dataset to mimic the WSR-88D-like coarser-temporal-resolution observations (even though spatial resolution differences exist between PAR and WSR-88D observations) and is designed to examine the differences in the analyses and forecasts due to high-temporal-resolution PAR observations. All three experiments assimilate radar observations for a continuous 45-min DA period at every 5-min assimilation frequency. There are some missing PAR volume scans during this period. Finally, 1-h forecasts are launched at the end of the 15-, 30-, and 45-min assimilation periods, respectively. The goal is to evaluate how quickly and accurately the rapid-scan PAR observations can initialize and forecast the tornadic supercell storm.

The observation-space diagnostic statistics compared against the assimilated observations reveal that the filter shows no sign of forecast divergence during the 45-min assimilation period. All three experiments are able to analyze reflectivity structures that are similar to the observations even after a short 15-min DA period. The 15-min forecasts from the member closest to the ensemble mean largely captured the storm evolution, though storm A was too strong in the 0100 and 0115 UTC initializations. The 1-h forecast probabilities of low-level vorticity after 15, 30, and 45 min of DA from all three experiments indicate that the placement and alignment of the swath of high probabilities from the PAR experiment more closely match the WDSS-II-derived rotation track, particularly from the forecast initialized after only 30 min of DA. For this forecast, the low-level rotation from the WSR-88D does not cover the initial part of the WDSS-II rotation track, and the probability values from the PAR-reducedtilts experiment are comparatively low. The ETS score and the AUC also indicate that the PAR experiment forecasts showed improved skill compared with the WSR-88D and PAR-reducedtilts experiments, particularly over 15- and 30-min-long assimilation periods. The improved skill in the PAR experiment is the result of better capturing the southern extent of the reflectivity coverage in both storms A and B.

The overall results indicate that the WSR-88D and PAR-reducedtilts experiments perform most similarly to each other, and the PAR experiment performs better than those two experiments. From this, we conclude that the assimilation of high-frequency PAR observations results in improved accuracy over traditional WSR-88D observations. Furthermore, we conclude that this improvement in accuracy is the result of the increased data volume from the PAR. The improved accuracy is more pronounced with a short or moderately long (15–30 min) assimilation period. The positive impact of the higher temporal resolution of the PAR observations decreases for a longer assimilation period (45 min in this study). This is similar to the findings of the OSSE studies of Xue et al. (2006) and Yussouf and Stensrud (2010).

The ultimate goal of storm-scale radar DA and forecasts is to extend severe weather warning lead times (Stensrud et al. 2009). Within the context of the WoF paradigm, the overall results obtained from this study provide reasons for cautious optimism. A hypothetical real-time prediction system would require at least 12 volume scans, or about 45 min of operational WSR-88D data, to produce a reasonably good forecast. In contrast, the length of the NWRT PAR data assimilation period could be reduced to as little as 15 min, potentially increasing severe weather forecast lead times. These rapid-scan observations would be particularly beneficial in a rapidly evolving severe weather situation. The results from this study are consistent with the findings from the OSSE study in Yussouf and Stensrud (2010). However, the case we used for this study involves only two supercell storms. To lay a foundation for the value of the next-generation PAR technology beyond the current WSR-88D network in storm-scale modeling, more rigorous testing on how to best assimilate PAR observations in a variety of severe weather systems (e.g., quasi-linear convective systems, microbursts, hailstorms, nontornadic as well as tornadic supercell storms, etc.) is still needed. Additionally, the impact of the unique flexible adaptive scanning capability from NWRT PAR [e.g., dense vertical scanning and elevation prioritized scanning strategies; Heinselman and Torres (2011)], particularly when the storm is close to or far away from the radar, on the model analyses and forecasts also needs to be investigated. Moreover, errors in storm motion in storm-scale modeling warrant further investigation. Accurate forecasts of storm position are necessary for the skillful prediction of storm-associated hazards, a primary research goal of WoF.

REFERENCES

Aksoy, A., D. C. Dowell, and C. Snyder, 2009: A multicase comparative assessment of the ensemble Kalman filter for assimilation of radar observations. Part I: Storm-scale analyses. *Mon. Wea. Rev.*, **137**, 1805–1824, doi:10.1175/2008MWR2691.1.

——, ——, and ——, 2010: A multicase comparative assessment of the ensemble Kalman filter for assimilation of radar observations. Part II: Short-range ensemble forecasts. *Mon. Wea. Rev.*, **138**, 1273–1292, doi:10.1175/2009MWR3086.1.

Anderson, J. L., 2001: An ensemble adjustment Kalman filter for data assimilation. *Mon. Wea. Rev.*, **129**, 2884–2903, doi:10.1175/1520-0493(2001)129<2884:AEAKFF>2.0.CO;2.

Betts, A. K., 1973: A composite mesoscale cumulonimbus budget. *J. Atmos. Sci.*, **30**, 597–610, doi:10.1175/1520-0469(1973)030<0597:ACMCB>2.0.CO;2.

Bowden, K. A., P. L. Heinselman, D. M. Kingfield, and R. P. Thomas, 2015: Impacts of phased-array radar data on forecaster performance during severe hail and wind events. *Wea. Forecasting*, **30**, 389–404, doi:10.1175/WAF-D-14-00101.1.

Brewster, K., M. Hu, M. Xue, and J. Gao, 2005: Efficient assimilation of radar data at high resolution for short-range numerical weather prediction. *WWRP Int. Symp. on Nowcasting Very Short Range Forecasting*, Toulouse, France, WMO, 3.06. [Available online at http://twister.ou.edu/papers/BrewsterWWRP_Nowcasting.pdf.]

Brock, F. V., K. C. Crawford, R. L. Elliott, G. W. Cuperus, S. J. Stadler, H. L. Johnson, and M. D. Eilts, 1995: The Oklahoma Mesonet: A technical overview. *J. Atmos. Oceanic Technol.*, **12**, 5–19, doi:10.1175/1520-0426(1995)012<0005:TOMATO>2.0.CO;2.

Chou, M.-D., 1990: Parameterization for the absorption of solar radiation by O_2 and CO_2 with application to climate studies. *J. Climate*, **3**, 209–217, doi:10.1175/1520-0442(1990)003<0209:PFTAOS>2.0.CO;2.

——, 1992: A solar radiation model for use in climate studies. *J. Atmos. Sci.*, **49**, 762–772, doi:10.1175/1520-0469(1992)049<0762:ASRMFU>2.0.CO;2.

——, and M. J. Suarez, 1994: An efficient thermal infrared radiation parameterization for use in general circulation models. NASA Tech. Memo. 104606, Vol. 3, 85 pp. [Available online at https://ntrs.nasa.gov/search.jsp?R=19950009331.]

Curtis, C. D., and S. M. Torres, 2011: Adaptive range oversampling to achieve faster scanning on the National Weather Radar Testbed Phased-Array Radar. *J. Atmos. Oceanic Technol.*, **28**, 1581–1597, doi:10.1175/JTECH-D-10-05042.1.

Dawson, D. T., II, M. Xue, J. A. Milbrandt, and M. K. Yau, 2010: Comparison of evaporation and cold pool development be-

tween single-moment and multimoment bulk microphysics schemes in idealized simulations of tornadic thunderstorms. *Mon. Wea. Rev.*, **138**, 1152–1171, doi:10.1175/2009MWR2956.1.

——, L. J. Wicker, E. R. Mansell, and R. L. Tanamachi, 2012: Impact of the environmental low-level wind profile on ensemble forecasts of the 4 May 2007 Greensburg, Kansas, tornadic storm and associated mesocyclones. *Mon. Wea. Rev.*, **140**, 696–716, doi:10.1175/MWR-D-11-00008.1.

——, M. Xue, J. Milbrandt, and A. Shapiro, 2015: Sensitivity of real-data simulations of the 3 May 1999 Oklahoma City tornadic supercell and associated tornadoes to multimoment microphysics. Part I: Storm- and tornado-scale numerical forecasts. *Mon. Wea. Rev.*, **143**, 2241–2265, doi:10.1175/MWR-D-14-00279.1.

Dowell, D. C., and L. J. Wicker, 2009: Additive noise for storm-scale ensemble data assimilation. *J. Atmos. Oceanic Technol.*, **26**, 911–927, doi:10.1175/2008JTECHA1156.1.

——, F. Zhang, L. J. Wicker, C. Snyder, and N. A. Crook, 2004: Wind and temperature retrievals in the 17 May 1981 Arcadia, Oklahoma, supercell: Ensemble Kalman filter experiments. *Mon. Wea. Rev.*, **132**, 1982–2005, doi:10.1175/1520-0493(2004)132<1982:WATRIT>2.0.CO;2.

——, G. S. Romine, and C. Snyder, 2010: Ensemble storm-scale data assimilation and prediction for severe convective storms. *25th Conf. on Severe Local Storms*, Denver, CO, Amer. Meteor. Soc., 9.5. [Available online at https://ams.confex.com/ams/25SLS/techprogram/paper_176121.htm.]

——, L. J. Wicker, and C. Snyder, 2011: Ensemble Kalman filter assimilation of radar observations of the 8 May 2003 Oklahoma City supercell: Influences of reflectivity observations on storm-scale analyses. *Mon. Wea. Rev.*, **139**, 272–294, doi:10.1175/2010MWR3438.1.

Du, J., J. McQueen, G. DiMego, Z. Toth, D. Jovic, B. Zhou, and H.-Y. Chuang, 2006: New dimension of NCEP Short-Range Ensemble Forecasting (SREF) system: Inclusion of WRF members. *WMO Expert Team Meeting on Ensemble Prediction Systems*, Exeter, United Kingdom, WMO. [Available online at http://www.emc.ncep.noaa.gov/mmb/SREF/WMO06_full.pdf.]

Emersic, C., P. L. Heinselman, D. R. MacGorman, and E. C. Bruning, 2011: Lightning activity in a hail-producing storm observed with phased-array radar. *Mon. Wea. Rev.*, **139**, 1809–1825, doi:10.1175/2010MWR3574.1.

Evensen, G., 1994: Sequential data assimilation with a nonlinear quasi-geostrophic model using Monte Carlo methods to forecast error statistics. *J. Geophys. Res.*, **99**, 10 143–10 162, doi:10.1029/94JC00572.

Fiori, E., A. Parodi, and F. Siccardi, 2010: Turbulence closure parameterization and grid spacing effects in simulated supercell storms. *J. Atmos. Sci.*, **67**, 3870–3890, doi:10.1175/2010JAS3359.1.

Forsyth, D. E., and Coauthors, 2005: The National Weather Radar Testbed (phased array). *32nd Conf. on Radar Meteorology*, Albuquerque, NM, Amer. Meteor. Soc., 12R.3. [Available online at https://ams.confex.com/ams/32Rad11Meso/techprogram/paper_96377.htm.]

Gaspari, G., and S. E. Cohn, 1999: Construction of correlation functions in two and three dimensions. *Quart. J. Roy. Meteor. Soc.*, **125**, 723–757, doi:10.1002/qj.49712555417.

Heinselman, P. L., and S. M. Torres, 2011: High-temporal-resolution capabilities of the National Weather Radar Testbed Phased-Array Radar. *J. Appl Meteor. Climatol.*, **50**, 579–593, doi:10.1175/2010JAMC2588.1.

——, D. L. Priegnitz, K. L. Manross, T. M. Smith, and R. W. Adams, 2008: Rapid sampling of severe storms by the National Weather Radar Testbed Phased Array Radar. *Wea. Forecasting*, **23**, 808–824, doi:10.1175/2008WAF2007071.1.

——, D. S. LaDue, and H. Lazrus, 2012: Exploring impacts of rapid-scan radar data on NWS warning decisions. *Wea. Forecasting*, **27**, 1031–1044, doi:10.1175/WAF-D-11-00145.1.

——, ——, D. M. Kingfield, and R. Hoffman, 2015: Tornado warning decisions using phased-array radar data. *Wea. Forecasting*, **30**, 57–78, doi:10.1175/WAF-D-14-00042.1.

Hong, S.-Y., and H.-L. Pan, 1996: Nonlocal boundary layer vertical mixing in a medium-range forecasting model. *Mon. Wea. Rev.*, **124**, 2322–2339, doi:10.1175/1520-0493(1996)124<2322:NBLVDI>2.0.CO;2.

Jung, Y., M. Xue, and M. Tong, 2012: Ensemble Kalman filter analyses of the 29–30 May 2004 Oklahoma tornadic thunderstorm using one- and two-moment bulk microphysics schemes, with verification against polarimetric radar data. *Mon. Wea. Rev.*, **140**, 1457–1475, doi:10.1175/MWR-D-11-00032.1.

Kain, J. S., and J. M. Fritsch, 1990: A one-dimensional entraining/detraining plume model and its application in convective parameterization. *J. Atmos. Sci.*, **47**, 2784–2802, doi:10.1175/1520-0469(1990)047<2784:AODEPM>2.0.CO;2.

——, and ——, 1993: Convective parameterization for mesoscale models: The Kain–Fritsch scheme. *The Representation of Cumulus Convection in Numerical Models*, *Meteor. Monogr.*, No. 46, Amer. Meteor. Soc., 165–170.

Kuster, C. M., P. L. Heinselman, and M. Austin, 2015: 31 May 2013 El Reno tornadoes: Advantages of rapid-scan phased-array radar data from a warning forecaster's perspective. *Wea. Forecasting*, **30**, 933–956, doi:10.1175/WAF-D-14-00142.1.

Lakshmanan, V., T. Smith, G. Stumpf, and K. Hondl, 2007: The Warning Decision Support System–Integrated Information. *Wea. Forecasting*, **22**, 596–612, doi:10.1175/WAF1009.1.

Lange, H., and G. C. Craig, 2014: The impact of data assimilation length scales on analysis and prediction of convective storms. *Mon. Wea. Rev.*, **142**, 3781–3808, doi:10.1175/MWR-D-13-00304.1.

Lei, T., M. Xue, and T. Yu, 2009: Multi-scale analysis and prediction of the 8 May 2003 Oklahoma City tornadic supercell storm assimilating radar and surface network data using EnKF. *13th Conf. on Integrated Observing and Assimilation Systems for Atmosphere, Oceans, and Land Surface (IOAS-AOLS)*, Phoenix, AZ, Amer. Meteor. Soc., 6.4. [Available online at https://ams.confex.com/ams/89annual/techprogram/paper_150404.htm.]

Lin, Y.-L., R. D. Farley, and H. D. Orville, 1983: Bulk parameterization of the snow field in a cloud model. *J. Climate Appl. Meteor.*, **22**, 1065–1092, doi:10.1175/1520-0450(1983)022<1065:BPOTSF>2.0.CO;2.

Mason, I. B., 1982: A model for the assessment of weather forecasts. *Aust. Meteor. Mag.*, **30**, 291–303.

Mason, S. J., and N. E. Graham, 1999: Conditional probabilities, relative operating characteristics, and relative operating levels. *Wea. Forecasting*, **14**, 713–725, doi:10.1175/1520-0434(1999)014<0713:CPROCA>2.0.CO;2.

McPherson, R. A., and Coauthors, 2007: Statewide monitoring of the mesoscale environment: A technical update on the Oklahoma Mesonet. *J. Atmos. Oceanic Technol.*, **24**, 301–321, doi:10.1175/JTECH1976.1.

Milbrandt, J. A., and M. K. Yau, 2006a: A multimoment bulk microphysics parameterization. Part III: Control simulation of a hailstorm. *J. Atmos. Sci.*, **63**, 3114–3136, doi:10.1175/JAS3816.1.

——, and ——, 2006b: A multimoment bulk microphysics parameterization. Part IV: Sensitivity experiments. *J. Atmos. Sci.*, **63**, 3137–3159, doi:10.1175/JAS3817.1.

Miller, M. L., V. Lakshmanan, and T. Smith, 2013: An automated method for depicting mesocyclone paths and intensities. *Wea. Forecasting*, **28**, 570–585, doi:10.1175/WAF-D-12-00065.1.

Newman, J. F., and P. L. Heinselman, 2012: Evolution of a quasi-linear convective system sampled by phased array radar. *Mon. Wea. Rev.*, **140**, 3467–3486, doi:10.1175/MWR-D-12-00003.1.

Potvin, C. K., and L. J. Wicker, 2013: Assessing ensemble forecasts of low-level supercell rotation within an OSSE framework. *Wea. Forecasting*, **28**, 940–960, doi:10.1175/WAF-D-12-00122.1.

Putnam, B. J., M. Xue, Y. Jung, N. Snook, and G. Zhang, 2014: The analysis and prediction of microphysical states and polarimetric radar variables in a mesoscale convective system using double-moment microphysics, multinetwork radar data, and the ensemble Kalman filter. *Mon. Wea. Rev.*, **142**, 141–162, doi:10.1175/MWR-D-13-00042.1.

Sakov, P., G. Evensen, and L. Bertino, 2010: Asynchronous data assimilation with the EnKF. *Tellus*, **62A**, 24–29, doi:10.1111/j.1600-0870.2009.00417.x.

Snook, N., M. Xue, and Y. Jung, 2011: Analysis of a tornadic mesoscale convective vortex based on ensemble Kalman filter assimilation of CASA X-band and WSR-88D radar data. *Mon. Wea. Rev.*, **139**, 3446–3468, doi:10.1175/MWR-D-10-05053.1.

——, ——, and ——, 2012: Ensemble probabilistic forecasts of a tornadic mesoscale convective system from ensemble Kalman filter analyses using WSR-88D and CASA radar data. *Mon. Wea. Rev.*, **140**, 2126–2146, doi:10.1175/MWR-D-11-00117.1.

——, ——, and ——, 2015: Multiscale EnKF assimilation of radar and conventional observations and ensemble forecasting for a tornadic mesoscale convective system. *Mon. Wea. Rev.*, **143**, 1035–1057, doi:10.1175/MWR-D-13-00262.1.

Snyder, C., and F. Zhang, 2003: Assimilation of simulated Doppler radar observations with an ensemble Kalman filter. *Mon. Wea. Rev.*, **131**, 1663–1677, doi:10.1175//2555.1.

Sobash, R. A., and D. J. Stensrud, 2015: Assimilating surface mesonet observations with the EnKF to improve ensemble forecasts of convection initiation on 29 May 2012. *Mon. Wea. Rev.*, **143**, 3700–3725, doi:10.1175/MWR-D-14-00126.1.

Stensrud, D. J., and J. Gao, 2010: Importance of horizontally inhomogeneous environmental initial conditions to ensemble storm-scale radar data assimilation and very short-range forecasts. *Mon. Wea. Rev.*, **138**, 1250–1272, doi:10.1175/2009MWR3027.1.

——, and Coauthors, 2009: Convective-scale warn-on-forecast system: A vision for 2020. *Bull. Amer. Meteor. Soc.*, **90**, 1487–1499, doi:10.1175/2009BAMS2795.1.

——, and Coauthors, 2013: Progress and challenges with Warn-on-Forecast. *Atmos. Res.*, **123**, 2–16, doi:10.1016/j.atmosres.2012.04.004.

Sun, W.-Y., and C.-Z. Chang, 1986: Diffusion model for a convective layer. Part I: Numerical simulation of convective boundary layer. *J. Climate Appl. Meteor.*, **25**, 1445–1453, doi:10.1175/1520-0450(1986)025<1445:DMFACL>2.0.CO;2.

Tanamachi, R. L., P. L. Heinselman, and L. J. Wicker, 2015: Impacts of a storm merger on the 24 May 2011 El Reno, Oklahoma, tornadic supercell. *Wea. Forecasting*, **30**, 501–524, doi:10.1175/WAF-D-14-00164.1.

Tong, M., and M. Xue, 2005: Ensemble Kalman filter assimilation of Doppler radar data with a compressible nonhydrostatic model: OSS experiments. *Mon. Wea. Rev.*, **133**, 1789–1807, doi:10.1175/MWR2898.1.

——, and ——, 2008: Simultaneous estimation of microphysical parameters and atmospheric state with radar data and ensemble square root Kalman filter. Part I: Sensitivity analysis and parameter identifiability. *Mon. Wea. Rev.*, **136**, 1630–1648, doi:10.1175/2007MWR2070.1.

Wang, S., M. Xue, and J. Min, 2013: A four-dimensional asynchronous ensemble square-root filter (4DEnSRF) algorithm and tests with simulated radar data. *Quart. J. Roy. Meteor. Soc.*, **139**, 805–819, doi:10.1002/qj.1987.

Wang, Y., Y. Jung, T. A. Supinie, and M. Xue, 2013: A hybrid MPI/OpenMP parallel algorithm and performance analysis for an ensemble square root filter suitable for dense observations. *J. Atmos. Oceanic Technol.*, **30**, 1382–1397, doi:10.1175/JTECH-D-12-00165.1.

Weber, M. E., J. Y. N. Cho, J. S. Herd, J. M. Flavin, W. E. Benner, and G. S. Torok, 2007: The next-generation multimission U.S. surveillance radar network. *Bull. Amer. Meteor. Soc.*, **88**, 1739–1751, doi:10.1175/BAMS-88-11-1739.

Wheatley, D. M., N. Yussouf, and D. J. Stensrud, 2014: Ensemble Kalman filter analyses and forecasts of a severe mesoscale convective system using different choices of microphysics schemes. *Mon. Wea. Rev.*, **142**, 3243–3263, doi:10.1175/MWR-D-13-00260.1.

Whitaker, J. S., and T. M. Hamill, 2002: Ensemble data assimilation without perturbed observations. *Mon. Wea. Rev.*, **130**, 1913–1924, doi:10.1175/1520-0493(2002)130<1913:EDAWPO>2.0.CO;2.

——, and ——, 2012: Evaluating methods to account for system errors in ensemble data assimilation. *Mon. Wea. Rev.*, **140**, 3078–3089, doi:10.1175/MWR-D-11-00276.1.

Wilks, D. S., 2006: *Statistical Methods in the Atmospheric Sciences.* 2nd ed. Elsevier, 627 pp.

Xu, X., M. Xue, and Y. Wang, 2015: Mesovortices within the 8 May 2009 bow echo over central United States: Analyses of the characteristics and evolution based on Doppler radar observations and a high-resolution model simulation. *Mon. Wea. Rev.*, **143**, 2266–2290, doi:10.1175/MWR-D-14-00234.1.

Xue, M., J. Zong, and K. K. Droegemeier, 1996: Parameterization of PBL turbulence in a multi-scale non-hydrostatic model. Preprints, *11th Conf. Numerical Weather Prediction*, Norfolk, VA, Amer. Meteor. Soc., 363–365.

——, K. K. Droegemeier, and V. Wong, 2000: The Advanced Regional Prediction System (ARPS)—A multi-scale non-hydrostatic atmospheric simulation and prediction tool. Part I: Model dynamics and verification. *Meteor. Atmos. Phys.*, **75**, 161–193, doi:10.1007/s007030070003.

——, and Coauthors, 2001: The Advanced Regional Prediction System (ARPS)—A multi-scale nonhydrostatic atmospheric simulation and prediction tool. Part II: Model physics and applications. *Meteor. Atmos. Phys.*, **76**, 143–166, doi:10.1007/s007030170027.

——, D.-H. Wang, J.-D. Gao, K. Brewster, and K. K. Droegemeier, 2003: The Advanced Regional Prediction System (ARPS), storm-scale numerical weather prediction and data assimilation. *Meteor. Atmos. Phys.*, **82**, 139–170, doi:10.1007/s00703-001-0595-6.

——, M. Tong, and K. K. Droegemeier, 2006: An OSSE framework based on the ensemble square-root Kalman filter for evaluating impact of data from radar networks on thunderstorm analysis and forecast. *J. Atmos. Oceanic Technol.*, **23**, 46–66, doi:10.1175/JTECH1835.1.

——, M. Hu, and A. Schenkman, 2014: Numerical prediction of the 8 May 2003 Oklahoma City tornadic supercell and embedded tornado using ARPS with the assimilation of WSR-88D data. *Wea. Forecasting*, **29**, 39–62, doi:10.1175/WAF-D-13-00029.1.

Yussouf, N., and D. J. Stensrud, 2010: Impact of phased-array radar observations over a short assimilation period: Observing system simulation experiments using an ensemble Kalman filter. *Mon. Wea. Rev.*, **138**, 517–538, doi:10.1175/2009MWR2925.1.

——, and ——, 2012: Comparison of single-parameter and multiparameter ensembles for assimilation of radar observations using the ensemble Kalman filter. *Mon. Wea. Rev.*, **140**, 562–586, doi:10.1175/MWR-D-10-05074.1.

——, E. R. Mansell, L. J. Wicker, D. M. Wheatley, and D. J. Stensrud, 2013: The ensemble Kalman filter analyses and forecasts of the 8 May 2003 Oklahoma City tornadic supercell storm using single- and double-moment microphysics schemes. *Mon. Wea. Rev.*, **141**, 3388–3412, doi:10.1175/MWR-D-12-00237.1.

——, D. C. Dowell, L. J. Wicker, K. H. Knopfmeier, and D. M. Wheatley, 2015: Storm-scale data assimilation and ensemble forecasts for the 27 April 2011 severe weather outbreak in Alabama. *Mon. Wea. Rev.*, **143**, 3044–3066, doi:10.1175/MWR-D-14-00268.1.

——, J. S. Kain, and A. J. Clark, 2016: Short-term probabilistic forecasts of the 31 May 2013 Oklahoma tornado and flash flood event using a continuous-update-cycle storm-scale ensemble system. *Wea. Forecasting*, **31**, 957–983, doi:10.1175/WAF-D-15-0160.1.

Zhang, J., and Coauthors, 2011: National Mosaic and Multi-Sensor QPE (NMQ) system: Description, results, and future plans. *Bull. Amer. Meteor. Soc.*, **92**, 1321–1338, doi:10.1175/2011BAMS-D-11-00047.1.

Zrnić, D. S., and Coauthors, 2007: Agile-beam phased array radar for weather observations. *Bull. Amer. Meteor. Soc.*, **88**, 1753–1766, doi:10.1175/BAMS-88-11-1753.